First-principles analysis of Catalysis for Hydrogen Evolution Reaction

A Thesis

Submitted in the partial fulfillment for the Degree of

MASTER OF SCIENCE

As a part of Integrated Ph.D. programme in

MATERIALS SCIENCE

by

Lakshay Dheer

CHEMISTRY AND PHYSICS OF MATERIALS UNIT
JAWAHARLAL NEHRU CENTRE FOR ADVANCED SCIENTIFIC RESEARCH
Bangalore - 560 064

March 2018

To my family

DECLARATION

I hereby declare that the matter embodied in the thesis entitled "**First-principles analysis of Catalysis for Hydrogen Evolution Reaction**" is the result of investigations carried out by me at the Chemistry and Physics of Materials Unit, Jawaharlal Nehru Centre for Advanced Scientific Research, Bangalore, India under the supervision of Prof. Umesh V. Waghmare and that it has not been submitted elsewhere for the award of any degree or diploma.

In keeping with the general practice in reporting scientific observations, due acknowledgement has been made whenever the work described is based on the findings of other investigators.

Lakshay Dheer

CERTIFICATE

I hereby certify that the matter embodied in this thesis entitled "**First-principles analysis of Catalysis for Hydrogen Evolution Reaction**" has been carried out by Mr. Lakshay Dheer at the Chemistry and Physics of Materials Unit, Jawaharlal Nehru Centre for Advanced Scientific Research, Bangalore, India under my supervision and that it has not been submitted elsewhere for the award of any degree or diploma.

Prof. Umesh V. Waghmare
(Research Supervisor)

Acknowledgements

First and foremost, I wish to express my heartfelt gratitude to my research supervisor Prof. Umesh V. Waghmare for his perennial guidance, invigoration and support throughout my research work. He provided me complete freedom in my work while teaching me to understand and appreciate the miniscule details in one's work. His positive view towards the world and limitless zeal to give his hundred percent has been exceptionally inspiring. It has been an honor to work in his shadow.

I am very lucky to have a wonderful bunch of people as my colleagues. All the members of Materials Theory Group have helped me in several ways and I have learned so much from them and am still learning. I would like to thank all my seniors, Dr. Koushik, Dr. Anjali, Dr. Arpita, Dr. Prasad, Dr. Sampath, Dr. Anuja, Dr. Sweta, Dr. Henu, Meha, Pawan, Suchitra, for teaching me almost everything I know. I have had a great time with all my other lab mates, Narendra, Shashank, Raagya and Shivani. A special thanks to Suchitra di for always helping me through the technicalities of the work.

I am grateful to Prof. Balasubramanian Sundaram, Prof. Chandrabhas Narayana, Prof. Eswaramoorthy M., Prof. Tapas Kumar Maji, Prof. Swapan K. Pati, Prof. Shobhana Narasimhan, Prof. Sundaresan A., Prof. Umesh V. Waghmare, Prof. K.S. Narayan, Prof. S.M. Shivaprasad, Prof. Vidhyadhiraja N.S., Prof. Sebastian C. Peter and Dr. Kanishka Biswas whose classes have taught me so much. It has been a pleasure to learn from all of them.

My integrated Ph.D. batch mates, Rajendra, Sukanya, Niloyendu, Janaky and Narendra made all the course work assignments and exams a fun activity. I wish to thank all of them for all the fun we had together during various experiments, assignments and otherwise. I really appreciate all the advice and guidance from my Integrated Ph.D. and Ph.D. seniors during my initial days of JNCASR.

I am also greatly thankful to our Lab Convenors and Mr. Ala Srinivas Rao for their help with instruments and measurements.

I have been blessed with some amazing people who have become an intimate part of my life. I would like to thank my close friends here in JNCASR who have always believed in me and supported every time. Hearty thanks you, Rajendra, Shashank, Neha,

Rukhsan and Ananya. I have learnt so much from them and our experiences together have made me a better person. A special thanks to Ananya for being a constant support and always pushing me to my limits. My journey till now has been pretty amazing thanks to these superb people in my life.

I would also like to thank my school friends with whom I have spent some of the best time of my life.

I am grateful to the Thematic Unit of Excellence on Computational Materials Science (TUE-CMS) for providing the computational resources. Special thanks to Prof. Bala and Vijay.

Lastly, I cannot begin to express my feelings towards all my lovely family members who have made everything possible for me. A big thanks to my family in Bangalore, Yanik and Ojaswi for all the dinners and hangouts. Their company made this new city feel like home. Maa and Papa have been a limitless source of constant support and energy in my life. They have raised me in the best way possible and have showered me with selfless love and have taught me how to be happy. Most importantly the biggest thanks to my brother Daksh, for inspiring me with his innocence and being the biggest motivation in my life. Thanks for making my reports grammatically accurate and being an honest critic.

Synopsis

With increasing global population, our long-term reliance on finite fossil energy is clearly unsustainable, both environmentally and economically. In recent times, climbing prices of oil have drawn attention to the energy-security risks of relying on these non-renewable sources, rushing the need to move to more secure and sustainable energy technologies. Hydrogen tops the list of potential replacements for oil and gas in the energy economy. Preferred production techniques for hydrogen are the ones which use renewable sources of energy. Electrolysis of water is referred to as water splitting and comprises of two half-cell reactions, one of which gives hydrogen (H_2) as the product. Designing catalysts that efficiently reduce H^+ ions to produce H_2 has been an active area in the scientific community for decades now. Presently platinum group metals are state-of-the-art materials to execute the hydrogen evolution reaction (HER). Being scarce and expensive, it is not feasible to generalize them for practical applications. Low-cost materials as alternatives to platinum group metals for HER catalysts are being explored in order to realize hydrogen as the modern-day fuel.

In this thesis, we use density functional theory (DFT) in order to study the catalytic performance of two materials, a van der Waals hetero-structure comprising of (N) graphene and a transition metal dichalcogenide (MoS_2), and an earth abundant metal-based alloy of Co-Mo-P.

We study the effect of doping nitrogen (N) of different chemical nature on the electronic, structural and catalytic properties of the graphene:1H-MoS_2 hetero-structure. We show that these vdW hetero-structures, have potential to be used as catalysts for reducing H^+ ions and the catalytic activity is strongly influenced by the type of N-atom doped in the graphene layer. The electronic structure of the hetero-structure is majorly affected by the chemical identity of N.

We examine the catalytic activity of an alloy comprising of cobalt (Co), molybdenum (Mo) and phosphorus (P) for alkaline HER using DFT. We show that synergy between Mo and P effectively tunes the energetics of the HER reaction intermediates giving rise to the excellent catalytic activity of Co-Mo-P alloy. The Co-Mo-P alloy effectuates the steps of HER with each atom playing an important role.

List of Figures

1.1 Mechanism of hydrogen evolution reaction on the surface of an electrode in acidic solution. The blue, red and purple arrows correspond to the *Volmer*, *Tafel* and *Heyrovsky* steps, respectively. 4

1.2 Volcano plot of experimentally measured exchange current density as a function of DFT calculated Gibbs free energy of adsorbed H-atom. 5

2.1 Self-consistency loop for the iterative solution of the KS equation. 15

3.1 Top and side view of constructed hetero-structure, (a) Pristine graphene:MoS_2, (b) graphitic N-graphene:MoS_2, (c) pyridinic N-graphene:MoS_2, and (d) pyrrolic N-graphene:MoS_2. Grey, blue, cyan, yellow and green spheres represent carbon, nitrogen, molybdenum, sulfur and hydrogen atoms respectively. 22

3.2 Binding energy (E_b) versus interlayer spacing between the two monolayers. 24

3.3 Schematic representation of (a) graphitic N-graphene:MoS_2, (b) pyridinic N-graphene:MoS_2, and (c) pyrrolic N-graphene:MoS_2. Carbon, nitrogen and hydrogen atoms are represented by grey, blue and green spheres respectively. 25

3.4 Electronic structure and projected density of states (PDoS) of (a) Pristine graphene:MoS_2, (b) G N-graphene:MoS_2, (c) Pn N-graphene:MoS_2, and (d) Pr N-graphene:MoS_2. We note an overlapping electronic structure of graphene and MoS_2 (a), n-type character in graphitic N-doped graphene:MoS_2 (b), defect bands of N and p-type character in the valence band of graphene (c), and a gap opened up in graphene bands in (d). 27

3.5 Alignment of electronic bands of graphene (red) and MoS_2 (blue) with respect to standard hydrogen electrode (HER) and oxygen reduction potential (ORR) and vacuum. Green circles denote the Fermi energy. 29

3.6 Selected adsorption sites to study the adhesion of H-atom, OH and H_2O molecule for (a) Pristine graphene:MoS_2, (b) graphitic N-graphene:MoS_2, (c) pyridinic N-graphene:MoS_2, and (d) pyrrolic N-graphene:MoS_2 hetero-structures. Carbon, nitrogen and hydrogen atoms are represented by grey, blue and green spheres respectively. 30

3.7 Gibbs free energies of H-adsorption calculated for pristine and N-doped graphene:MoS_2 hetero-structures at various adsorption sites. 32

4.1 Generated $Co_{12}Mo_2P_2$ structures: (a) $Co_{12}Mo_2P_2$_Bulk_1; (b) $Co_{12}Mo_2P_2$_Bulk_2; (c) $Co_{12}Mo_2P_2$_Bulk_3; (d) $Co_{12}Mo_2P_2$_Bulk_4. Cobalt, molybdenum and phosphorus atoms are denoted as blue, purple and yellow spheres respectively. . . . 40

4.2 (2x2x1) Model amorphous structures of (a) $Co_{28}Mo_4P_4$ and (b) $Co_{12}Mo_2P_2$ obtained using the technique of expanded supercell and relaxation. Cobalt, molybdenum and phosphorus atoms are denoted as blue, purple and yellow spheres respectively. . . 42

4.3 The sites of adsorption on (a) $Co_{28}Mo_4P_4$ and (b) $Co_{12}Mo_2P_2$. Cobalt, molybdenum and phosphorus atoms are denoted as blue, purple and yellow spheres respectively. 43

4.4 Model structures of (a) $Co_{14}Mo_2$ and (b) $Co_{14}P_4$ obtained with 2x2x1 supercell. Cobalt, molybdenum and phosphorus atoms are represented with blue, purple and yellow spheres respectively. 44

4.5 **(a)** Splitting of H_2O molecules upon adsorption at the Mo-Co bridging site of (2x1x2) $Co_{28}Mo_4P_4$; **(b)** Energies of adsorption (E_{ads}) of H, OH and H_2O. Inset: A schematic showing the mechanism of how electronegative P-atom ionizes metal (M) and enhances OH-binding; **(c)** PDoS of OH (top) and H_2O (bottom) adsorbed on

$Co_{12}Mo_2P_2$, $Co_{14}Mo_2$, $Co_{14}P_2$; **(d)** Iso-surfaces of wave functions depicting the interacting orbitals (HOMO) for OH*$Co_{12}Mo_2P_2$ and H_2O*$Co_{12}Mo_2P_2$. Red and blue colors represent positive and negative iso-surfaces respectively. Co, Mo, P, O and H atoms are represented with blue, purple, yellow, red and cyan spheres respectively. 47

List of Tables

3.1 Interlayer binding energy calculated (E_b) with and without including vdW interactions. 24

3.2 Work function of hetero-structures of (pristine) N-doped graphene and 1H-MoS_2 28

3.3 Adsorption energy (ΔE_{ads}) for pristine and N-doped graphene:MoS_2 hetero-structures at various adsorption sites.. 31

4.1 Calculated formation energy values for various doped configurations of $Co_{14}Mo_2P_2$. 41

4.2 Adsorption energies of H, OH and H_2O molecule at various adsorption sites shown in Fig 4.3. 44

4.3 Adsorption energies of H, OH and H_2O molecule at the adsorption site **1** of $Co_{14}Mo_2$, $Co_{12}Mo_2P_2$ and $Co_{14}P_2$. 45

Contents

Acknowledgements iv

Synopsis v

List of Figures vii

List of Tables xi

1. Introduction 1

1.1. Hydrogen Economy 2

1.2. Mechanism of HER. 3

1.3. Catalysts for HER. 5

Bibliography 7

2. Theoretical Methods 9

2.1. Introduction 10

2.2. Density Functional Theory 12

2.3. Hohenberg-Kohn Theorems 13

2.4. Kohn-Sham Approach 14

2.5. Exchange-Correlation Energy Functional 16

2.6. Pseudopotentials 17

Bibliography 18

3. van der Waals hetero-structures of 1H-MoS_2 and N-doped Graphene for Catalysis of HER 19

3.1. Introduction 20
3.2. Computational Details 21
3.3. Constructing the Hetero-structures 22
3.4. Adhesion between the two Monolayers 23
3.5. Electronic Structure and Projected Density of States 25
3.6. Work Function 28
3.7. Catalysis of HER 29
3.8. Conclusions 32
Bibliography 34

4. Co-Mo-P alloy-based Catalyst for superior Alkaline HER: A first-principles study 37

4.1. Introduction 38
4.2. Computational Details 38
4.3. Generating Co-Mo-P Alloy 39
4.4. Constructing Amorphous Structures. 41
4.5. Reaction mechanism of Alkaline HER 42
4.6. Adsorption of H, OH and H_2O 42
4.7. Conclusions 47
Bibliography 49

Chapter 1

Introduction

1.1 Hydrogen Economy

Fossil fuels have been the backbone of the technologies powering the Industrial Revolution from early 18th century. Being limited in quantity, these sources of energies need to be replaced by renewable ones. Moreover, consumption of fuels like oil, coal and natural gas has been the main source of chemical pollutants like carbon dioxide (CO_2), which is directly associated with global warming. As of April 2017, CO_2 concentration reached 410 parts per million (ppm) as compared to 280 ppm in 1958 [1]. In less than 60 years CO_2 concentration increased by 50%, mostly driven by the enormous amounts of CO_2 we are generating by burning fossil fuels. Of all the proposed alternative options to fulfill energy demands across the globe, use of hydrogen (H_2) appears to be the most viable option. It is the only known fuel to have zero carbon dioxide (CO_2) emission as well as the highest gravimetric energy density [2]. Despite its benefits, the main challenge keeping hydrogen dormant in practical application is the lack of sustainable production methods. As of now, almost all of the H_2 is generated by steam-reforming of fossil fuels [3] which releases CO_2 as a by-product making it non-viable. Clean and sustainable methods of H_2 synthesis are being explored extensively so as to realize the "Hydrogen Economy" [4]. One of the clean methods to generate H_2 is by electrolysis of water, preferably using solar energy [3].

$$H_2O + \text{energy} \longrightarrow H_2 + 0.5O_2$$

Two half-cell reactions together constitute the electrochemical water splitting

- Oxygen evolution reaction (OER)

$$2H_2O\ (l) \longrightarrow O_2\ (g) + 4H^+\ (aq) + 4e^-$$

- Hydrogen evolution reaction (HER)

$$2H^+\ (aq) + 2e^- \longrightarrow H_2\ (g)$$

'Overpotential' is defined as the difference between applied and thermodynamic potentials for a given electrochemical reaction. In many reaction, electrodes do not behave ideally, as sometimes gaseous products obtained from the reaction get adsorbed on the electrode surface resulting in reduced activity. To overcome the sluggish kinetics an extra potential is applied, referred to as overpotential. In an ideal scenario, the energy required to generate one molecule of H_2 and O_2 from one molecule of H_2O under STP conditions is equivalent to a cell voltage of 1.23 V. In practice, however, the electrolysis

of water is less efficient and external potentials are needed to carry out the reaction. This extra potential, called the overpotential, is needed to enhance the kinetics of the reaction by increasing the rate of electron transfer processes. This is where catalysts, photocatalysts and electrocatalysts, play a significant role. These compounds do not participate in the reaction themselves but lower the overpotentials, thereby executing the reaction more effectively.

1.2 Mechanism of HER

HER can be mechanistically described by two schemes [3]:

(i) Volmer-Tafel mechanism

(ii) Volmer-Heyrovsky mechanism

Step 1

Irrespective of the mechanism, the first step of HER is the *Volmer* step, also referred to as the *discharge* step. This step involves adsorption of a proton (H^+) on an empty active site of the catalyst facilitated by an electron transfer from the electrode (Fig 1.1). HER follows the same mechanism in acidic as well as alkaline media, the only difference being the source of proton. In an acidic solution, the hydronium ion (H_3O^+) donates the proton which then gets adsorbed on the catalyst's surface. When HER is carried out in an alkaline medium, the main source of protons is water molecule (H_2O).

Step 2

In the second step, two H-atoms combine to form an H_2 molecule which then desorbs from the surface leaving the catalyst unaltered (Fig 1.1). This may occur via two dissimilar reaction pathways.

• ***Heyrovsky*** **step:** In this step, another proton from the solution binds to the adsorbed H-atom, facilitated by a second electron transfer from the electrode. This leads to formation of an H_2 molecule which is then desorbed from the surface. This step is also known as *ion* + *atom* reaction.

• ***Tafel* step:** Also referred to as the *combination* reaction, here two H-atoms adsorbed in the vicinity of each other end up combining on the surface of the electrode forming H_2 molecule. This H_2 molecule then gets desorbed from the surface.

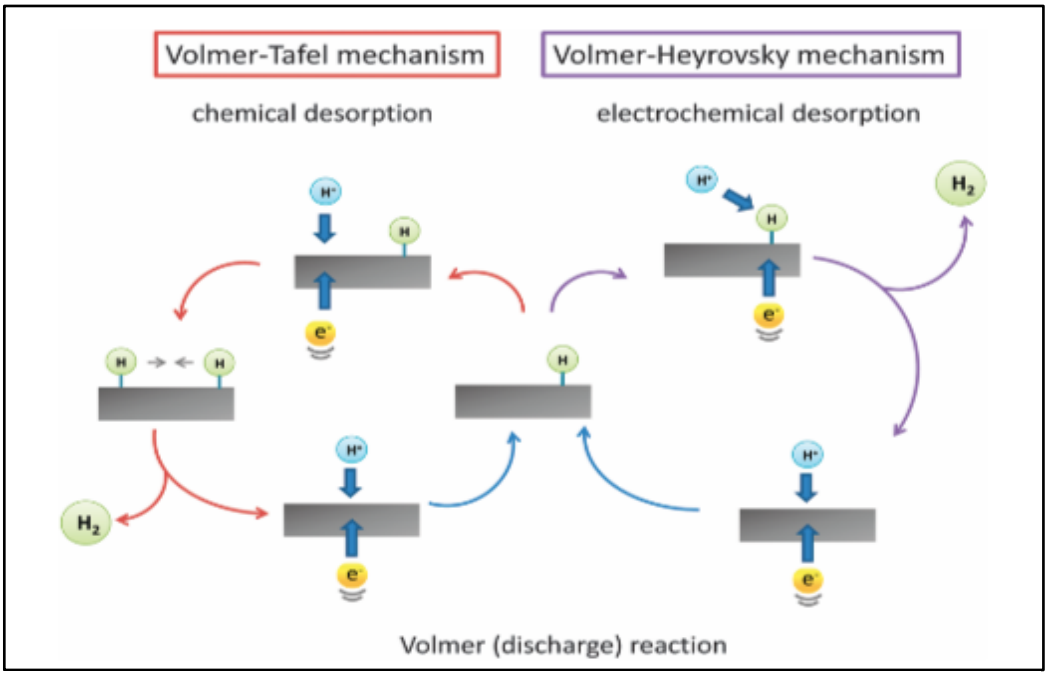

Figure 1.1 Mechanism of hydrogen evolution reaction on the surface of an electrode in acidic solution. The blue, red and purple arrows correspond to the *Volmer*, *Tafel* and *Heyrovsky* steps, respectively [3].

Designing catalysts that efficiently reduce H^+ ions at low overpotentials has been an active area in the scientific community for decades now. The most effective materials for this constitute precious metals like platinum but such a technology cannot be realized for practical application due to the expense associated with Pt as well its paucity. Other classes of promising HER electrocatalysts that have been developed include [5], non-precious transition metals, metal free catalysts, transition-metal phosphides, etc.

In order to design new and cheap catalysts to replace Pt, a descriptor-based approach can be implemented. One widely accepted descriptor of the catalytic activity of a material is the Gibbs free energy for hydrogen adsorption (ΔG_{H^*}) [3].

Volcano plot of exchange current density versus Gibbs free energy of the adsorbed H-atom demonstrates the Sabatier principle. Pt sits on top of the volcano with a ΔG_{H^*} value of ~ 0 eV. The metals on the left of Pt have a negative ΔG_{H^*} showing that H-atoms adhere

too strongly to the surface resulting in blocking of active sites. These blocked catalytic sites in turn lead to lowering of H_2 evolution. Having a positive value of ΔG_{H^*}, the metals to the right of Pt interact with H-atoms too weakly. This leads to destabilization of the intermediate state and inhibiting the overall reaction. Thus a ΔG_{H^*} value close to ~ 0 eV is desirable for a material to be effective in catalysing HER.

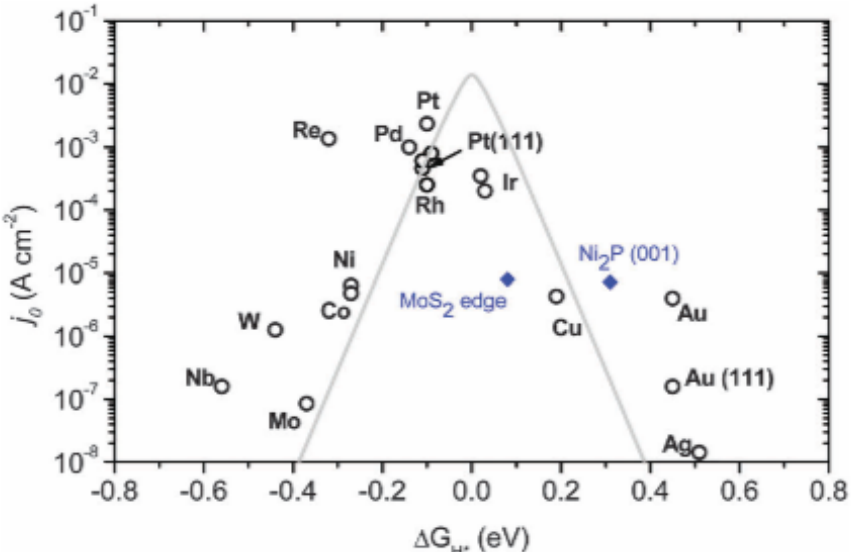

Figure 1.2 Volcano plot of experimentally measured exchange current density as a function of DFT-calculated Gibbs free energy of adsorbed H-atom [3].

1.3 Catalysts for HER

At present, platinum and platinum group metals are the best available electrocatalysts for HER. However, the expense associated with these metals and their low abundance minimize their widespread application. Hence, there is a global need to discover new cost-effective materials and optimize their ability to drive the HER. Tremendous efforts have been made over the last decade in this area with numerous reports, experimental as well as theoretical. This thesis focusses on investigation of two inexpensive catalysts for HER and their catalytic activity using first-principles calculations based on the density functional theory (DFT).

We have organized the rest of thesis as follows:

In **Chapter 2** we discuss the methods and formalism used in our calculations. Theoretical aspects of density functional theory (DFT) and various approximations and limitations of these theoretical techniques are highlighted in this chapter. **Chapter 3** includes a detailed theoretical analysis of N-doped graphene:MoS_2 hetero-structures, consisting of different chemical types of N: (i) Graphitic (G), (ii) Pyridinic (Pn), and (iii) Pyrrolic (Pr), with main focus on the effect of chemical nature of N on the catalytic activity of graphene:MoS_2 hetero-structure for HER. In **Chapter 4** we investigate a nonprecious metal-based catalyst for alkaline constituting cobalt (Co), molybdenum (Mo) and phosphorus (P). It is shown that synergy between Mo and P effectively tunes the energetics of the HER reaction intermediates giving rise to the excellent catalytic activity of Co-Mo-P alloy in alkaline medium.

Bibliography

[1] https://www.climatecentral.org/news/we-just-breached-the-410-parts-per-million-threshold-21372

[2] Min Zeng and Yanguang Li, *J. Mater. Chem. A* **3**, 14942 (2015).

[3] Carlos G. Morales-Guio, Lucas-Alexandre Stern and Xile Hu, *Chem. Soc. Rev.* **43**, 6555 (2014).

[4] Bockris, J. O'm.,Energy: The solar-hydrogen alternative, New York, Halsted Press, 1975. **381 p**.

[5] R. Subbaraman, D. Tripkovic, D. Strmcnik, K.-C. Chang, M. Uchimura, A. P. Paulikas, V. Stamenkovic and N. M. Markovic, *Science* **334**, 1256 (2011).

Chapter 2

Theoretical Methods

2.1 Introduction

Any property exhibited by a material arises due to the interaction between the electrons, the ions and the interaction among themselves. Quantum theory very accurately describes the behavior of these atomic and subatomic particles. The success of quantum theory has made it possible for scientists to explain and predict various properties of a material in solid state physics. Nearly all physical properties of a material are related to the total energy or the difference between total energies of the electrons and ions. In order to obtain the total energy of a system containing electrons and ions, one needs to solve the Schrödinger equation. The Hamiltonian of a system which takes into account electron-electron, electron-nuclear and nuclear-nuclear interactions is given by:

$$\widehat{H} = -\frac{\hbar^2}{2m_e}\sum_i \nabla_i^2 - \sum_{i,I}\frac{Z_I e^2}{|\boldsymbol{r}_i - \boldsymbol{R}_I|} + \frac{1}{2}\sum_{i\neq j}\frac{e^2}{|\boldsymbol{r}_i - \boldsymbol{r}_j|} - \sum_I \frac{\hbar^2}{2M_I} + \frac{1}{2}\sum_{I\neq J}\frac{Z_I Z_J e^2}{|\boldsymbol{R}_I - \boldsymbol{R}_J|} \tag{2.1}$$

where electrons are denoted by lowercase subscripts and nuclei, with charge Z_I and mass M_I, denoted by uppercase subscripts. The first term in Equation 2.1 is the kinetic energy of electrons, the second term represents the interaction between electrons and nuclei (termed as external potential), the third term is the interaction between electrons, the fourth term is the kinetic energy of nuclei and the fifth term is the interaction between nuclei. Given this total Hamiltonian of any system, we can write the time-independent Schrödinger equation as,

$$\widehat{H}\psi\,(\boldsymbol{R},\boldsymbol{r}) = \varepsilon\,\psi\,(\boldsymbol{R},\boldsymbol{r}) \tag{2.2}$$

$\boldsymbol{r} \equiv \{\boldsymbol{r}_1, \boldsymbol{r}_2, \boldsymbol{r}_3, \ldots\ldots\ldots\ldots, \boldsymbol{r}_N\}$ is the set of N electronic coordinates.

$\boldsymbol{R} \equiv \{\boldsymbol{R}_1, \boldsymbol{R}_2, \boldsymbol{R}_3, \ldots\ldots\ldots\ldots, \boldsymbol{R}_P\}$ is the set of P nuclear coordinates.

Where ε's are energy eigenvalues and ψ ***(R, r)***$'$s are the corresponding wave functions. ψ is asymmetric with respect to exchange of electronic coordinates in r and asymmetric or symmetric with respect to exchange of nuclear variables in R.

As a material has very large number of ions and electrons and their degrees of freedom are coupled to each other, we will have a very complicated coupled differential equation which will be impossible to solve, no matter how powerful a computer we have, unless we resort to some reasonably good approximations.

Also called the *Adiabatic approximation* [1], the *Born-Oppenheimer* approximation is the most important assumption made to simplify the calculation of electronic structure of matters. The basis of this assumption is based on the fact that time scale associated with the motion of the nuclei (ions) are much slower than that associated with electrons. Therefore, electrons instantaneously follow the motion of the ions while remaining in the same stationary (adiabatic) state (ground or excited) without causing non-radiative transition by the nuclear dynamics.

The mass of nucleus is approximately >1837 times larger than that of an electron, and hence its kinetic energy can be neglected. The *Born-Oppenheimer* approximation reduces equation 2.1 to :

$$\hat{H} = \hat{T} + \hat{V}_{ext} + \hat{V}_{int} + E_{II} \tag{2.3}$$

where $\hat{T}$ is the kinetic energy operator, $\hat{V}_{ext}$ is the potential acting on electrons due to nuclei, $\hat{V}_{int}$ is the electron-electron interaction and E_{II} is the classical interaction of nuclei with one another.

Various other approximations have also been developed to solve it. Independent electron approximation is the oldest approximation which considers that interaction between the electrons can be ignored. *Hartree* approximation modified it further by treating the electrons as independent, but interacting only via the mean-field Coulomb potential. Hartree did not consider the asymmetric nature of electronic wave functions. Anti-symmetric nature of electrons was considered in the *Hartree-Fock* Approximation.

2.2 Density Functional Theory

According to quantum mechanics wave function of a given system ψ, contains all the possible information about that system. The solution to this wave function is calculated by using the Schrödinger's equation (SE) which for a single electron moving in a potential $\upsilon(\boldsymbol{r})$ is given by:

$$\left[-\frac{\hbar^2\nabla^2}{2m}+\ \upsilon(\boldsymbol{r})\right]\psi\ (\boldsymbol{r})=\ \varepsilon\ \psi\ (\boldsymbol{r}) \tag{2.4}$$

For a many electron system, the SE becomes:

$$\left[\sum_{i}^{N}\left(-\frac{\hbar^2\nabla_i^2}{2m}+\ \upsilon(\boldsymbol{r_i})\right)+\ \sum_{i<j}U(\boldsymbol{r_i},\boldsymbol{r_j})\right]\psi\ (\boldsymbol{r_1},\boldsymbol{r_2}\ldots,\boldsymbol{r_N}) \tag{2.5}$$

$$=\ \varepsilon\psi\ (\boldsymbol{r_1},\boldsymbol{r_2}\ldots,\boldsymbol{r_N})$$

Where N is the number of electrons and $U(\mathbf{r}_i, \mathbf{r}_j)$ is the electron-electron interaction. In quantum mechanics, the usual approach to SE is as follows:

$$\boxed{\upsilon(\boldsymbol{r})\ \overset{SE}{\Rightarrow}\psi\ (\boldsymbol{r_1},\boldsymbol{r_2}\ldots,\boldsymbol{r_N})\ \overset{\langle\psi|\ldots|\psi\rangle}{\Longrightarrow}\ \text{observables}} \tag{2.6}$$

i.e., the system is specified by choosing $\upsilon(\boldsymbol{r})$ for which the SE is solved for wave function $\psi\ (\boldsymbol{r_1},\boldsymbol{r_2}\ldots,\boldsymbol{r_N})$. Expectation values of operators with this wave function is calculated to obtain various observables. One such observable is the particle density given by:

$$n(\boldsymbol{r})=N\int d^3\boldsymbol{r}_2\int d^3\boldsymbol{r}_3\ldots\int d^3\boldsymbol{r}_N\ \psi^*\ (\boldsymbol{r_1},\boldsymbol{r_2}\ldots,\boldsymbol{r_N})\ \psi(\boldsymbol{r_1},\boldsymbol{r_2}\ldots,\boldsymbol{r_N}) \tag{2.7}$$

The density functional theory (DFT) uses this particle density as the key variable to calculate all other observables. It has excluded the problem of 3N-variables (N is the number of electrons and their associated 3 spatial variables) associated with many

electron-wave function with a functional of electron density which reduces the number of variables to 3, and hence has reduces the complexity of many electron problem to a great extent. In other words, it allows one to map exactly the problem of strongly interacting electron gas onto that of a single particle moving in an effective potential arising from the rest. This approach can be summarized as follows:

$$n(\boldsymbol{r}) \Longrightarrow \psi\,(\boldsymbol{r_1}, \boldsymbol{r_2} \ldots, \boldsymbol{r_N}) \Longrightarrow \upsilon(\boldsymbol{r}) \tag{2.8}$$

2.3 Hohenberg-Kohn Theorems

Hohenberg and Kohn formulated density functional theory (DFT) in 1964 as an exact many-body theory. They proved two theorems [2] which established DFT as a rigorous quantum chemical methodology. The theorems are stated below:

Theorem I

The external potential $V_{\text{ext}}(\mathbf{r})$ of an interacting particle system is uniquely determined by the ground state density $n_o(\mathbf{r})$, within a constant.

Theorem II

The universal energy functional E[n] can be defined in terms of density $n_o(\mathbf{r})$ for any external potential $V_{ext}(\mathbf{r})$. The global minimum value of this functional is the ground state energy of the system for any $V_{ext}(\mathbf{r})$. The density $n_o(\mathbf{r})$ that minimizes it is the ground state density n_o(r).

The properties like the kinetic energy, etc., can be determined uniquely if $n(\mathbf{r})$ is specified, then each such property can be viewed as a functional of $n(\mathbf{r})$, including the total energy functional.

$$E_{HK}[n] = F_{HK}[n] + \int d^3\boldsymbol{r} V_{ext}(\boldsymbol{r}) n(\boldsymbol{r}) + E_{II} \tag{2.9}$$

E_{II} is the interaction energy of nuclei. Functional F_{HK}[n] includes all internal energies, kinetic energies and potential of interacting electron system and is given by:

$$F_{HK}[n] = T[n] + E_{int}[n] \tag{2.10}$$

F_{HK}[n] is universal by construction since the kinetic energy and interaction energy of the particles are both functional of density.

2.4 Kohn-Sham Approach

In order to evaluate the kinetic energy exactly, the only known practical way is to revert to the usual expression in terms of set of N wave functions. There is no known explicit functional to go directly from the density to the kinetic energy. A more general approach was suggested by Kohn and Sham (1965) [3]. In their approach, the unknown Hohenberg-Kohn functional is nothing but the kinetic energy of the electrons. The idea of Kohn-Sham was that if one can find any non-interacting electronic system that produces the same electronic density as that of the interacting system, then the kinetic energy of the electrons can be calculated through one electron orbitals. Using Kohn-Sham approach the energy functional can now be written as:

$$E[n(\boldsymbol{r})] = T_S[n(\boldsymbol{r})] + \frac{1}{2}\int \frac{n(\boldsymbol{r})n(\boldsymbol{r}')d^3\boldsymbol{r}d^3\boldsymbol{r}'}{|\boldsymbol{r}-\boldsymbol{r}'|} + \int drV_{ext}(\boldsymbol{r})n(\boldsymbol{r}) + E_{xc}[n(\boldsymbol{r})] \tag{2.11}$$

The first term is the kinetic energy of electrons, the second term is the electrostatic interaction energy between electrons, the third term is the interaction energy of electrons with external potential and the fourth term is the exchange-correlation interaction between electrons.

Here, the electron density is:

$$n(\boldsymbol{r}) = \sum_i |\psi_i(\boldsymbol{r})|^2 \tag{2.12}$$

In equation 2.11 $E_{xc}[n(\boldsymbol{r})]$, is the exchange-correlation energy functional. Taking functional derivative $\delta E_{xc}[n(\boldsymbol{r})]/\delta\,\psi_i^*$ with the constraint that each $\psi_i(\boldsymbol{r})$ normalized to units gives us:

$$\left[-\frac{\hbar^2}{2m}\nabla_i^2 + V_{KS}(\boldsymbol{r})\right]\psi_i(\boldsymbol{r}) = \varepsilon_i\,\psi_i(\boldsymbol{r}) \tag{2.13}$$

where, V_{KS} is the Kohn-Sham potential for the non-interacting system given as:

$$V_{KS}(\boldsymbol{r}) = V_{ext}(\boldsymbol{r}) + \int \frac{n(\boldsymbol{r}')}{|r-\boldsymbol{r}'|}d\boldsymbol{r}' + V_{xc}[n(\boldsymbol{r})] \tag{2.14}$$

where the first term is the external potential, the second term is the Hartree potential and the last term is the exchange-correlation potential, which is:

$$V_{xc}[n(\boldsymbol{r})] = \frac{\delta E_{xc}[n(\boldsymbol{r})]}{\delta n(\boldsymbol{r})} \tag{2.15}$$

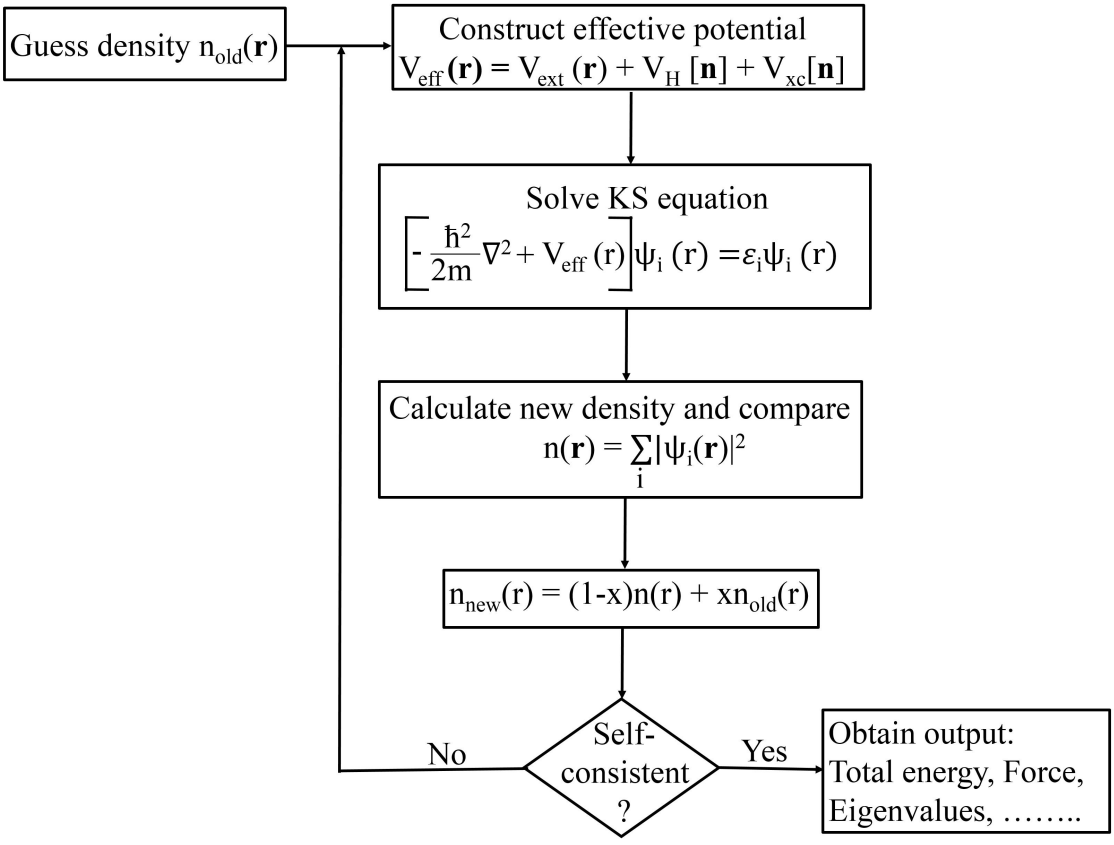

Figure 2.1 Self-consistency loop for the iterative solution of the KS equation.

2.5 Exchange-Correlation Energy Functional

Formulation of a correct exchange-correlation functional is one of the main drawbacks in the density functional theory. The local density approximation (LDA) and generalized gradient approximation (GGA) are the most popular and widely used among the available functionals.

In LDA, the exchange-correlation energy of an electronic system is constructed by assuming that the exchange-correlation energy per electron ($\varepsilon_{xc}(\boldsymbol{r})$) at a point $\boldsymbol{r}$ in the electron gas is equal to the exchange-correlation energy per electron of a homogenous electron gas that has the same density as the electron density at a point $\boldsymbol{r}$. Thus,

$$E_{xc}^{LDA}[n(\boldsymbol{r})] = \int \varepsilon_{xc}(\boldsymbol{r})\, n(\boldsymbol{r}) d^3\boldsymbol{r} \tag{2.16}$$

Using equation 2.16 and 2.14

$$\frac{\delta E_{xc}^{LDA}[n(\boldsymbol{r})]}{\delta n(\boldsymbol{r})} = \frac{\partial [n(\boldsymbol{r})\varepsilon_{xc}(\boldsymbol{r})]}{\partial n(\boldsymbol{r})} \tag{2.17}$$

where,

$$\varepsilon_{xc}(\boldsymbol{r}) = \varepsilon_{xc}^{hom}[n(\boldsymbol{r})] \tag{2.18}$$

The LDA approximation proves to be very successful for many systems especially for those whose electron density is quite uniform such as bulk metals, ionic crystals etc. But it fails to produce some properties (e.g. band gap) in semiconductors, strongly correlated systems due to fact that the excitation spectrum of homogeneous electron gas is gap-less and exchange-correlation energy is regular [4]. LDA also fails to capture weak inter-molecular bonds, hydrogen bonds etc.

GGA is an improved version of the LDA in which several aspects which were not present in LDA like inhomogeneity of electrons, non-local exchange correlation effect, complete cancellation of self-energies of electrons are taken into account. The exchange-correlation energy in GGA [5] can be written as:

$$E_{xc}^{GGA}[n(\boldsymbol{r})] = \int d^3\boldsymbol{r} n(\boldsymbol{r}) \varepsilon_{xc}\,[n(\boldsymbol{r}), |\nabla n|, |\nabla^2 n|, \ldots] \qquad (2.19)$$

The GGA method turns out to be better than LDA in the sense that it improves binding energies, bond lengths and also improves the band gap of semiconductors over LDA. For all these reasons, we implement GGA as exchange-correlation functional in all the ab-initio calculations described in this thesis.

2.6 Pseudopotentials

The core electrons in solids or molecules are tightly bound to the nucleus and are thus not involved in bonding. So, as an approximation core electrons are removed from the calculation, and the interaction of the valence electrons with the nucleus plus the core states is replaced by an effective screened potential. The solution of the atomic Schrödinger's equation for the pseudopotential is a pseudo-wave function different from the true wave function. The pseudopotential is constructed in such a way that its scattering properties are similar to those of the all-electron potential. It requires less number of basis functions and hence is computationally efficient, without compromising much on the properties of system.

A cutoff radius (r_c) is used to construct pseudopotentials which sort of separates the valence region from the core region. The region beyond r_c is treated as a valence region and within the r_c is core region. Pseudopotential and all electron wave function are identical outside the cutoff radius. In the norm conserving pseudopotentials, the norm of all electron wave function in the core region (0 to r_c) remains conserved. The norm conserving pseudopotential is not much effective in reducing the number of plane waves required for representation. A better alternative to this is the ultrasoft pseudopotential. The ultrasoft pseudopotential generates the smoother wave function and reduces the size of required plane wave basis set, by increasing the value of r_c without sacrificing transferability.

Bibliography

[1] M. Born and J R Oppenheimer, *Ann. Physik* **84**, 457 (1927).

[2] P. Hohenberg and W. Kohn, *Phys. Rev.* **136**, 864 (1964).

[3] W. Kohn and L. J. Sham, *Phys. Rev. A* **140**, 1133 (1965).

[4] J. Kohanoff, Electronic Structure Calculations for Solids and Molecules, Cambridge University Press, Cambridge (2006), ISBN:13-978-0-521- 81591-8.

[5] R. M. Martin, Electronic Structure, Basic Theory and Practical Methods, Cambridge University Press, Cambridge (2004), ISBN: 978-0-521-78285- 6.

Chapter 3

van der Waals hetero-structure of 1H-MoS_2 and N-doped Graphene for catalysis of HER

3.1 Introduction

Graphene [1], a 2-dimensional sheet of sp^2 hybridised carbon atoms, has been the kernel of research in the field of 2D materials since its isolation in 2004. Due to its unique electronic structure, graphene exhibits properties such as high electrical and thermal conductivities [2, 3], good transparency [4], great in-plane mechanical strength [5] and a large specific surface area [6]. Being atomically thick, graphene serves as a perfect candidate to form hetero-structure with other 2D materials. Molybdenite (MoS_2) [7], a Transition Metal Dichalcogenide (TMDC), is widely used in solid-state lubricants, photovoltaic devices and rechargeable batteries [8]. 2H-MoS_2 comprises of S-Mo-S layers which are held together by van der Waals interactions [9].

Recently, exciting research has centred on hybrid structures by combining different 2D materials together [10]. One can either couple these 2D crystals in a horizontal fashion creating an in-plane interface or by piling them on top of one another forming hetero-structures. An attractive feature of these hetero-structures is that each layer acts as the bulk material and the interface simultaneously [11]. These vertical heterojunctions are held together by van der Waals interactions and are known to showcase novel interface-induced physical and chemical properties [12]. A particularly well-studied hetero-structure is graphene:MoS_2 hybrid [12, 13, 14, 15] which was first fabricated by Chang *et al*. [16]. This stacked hetero-structure has recently been exploited for its catalytic activity. In a recent report the graphene:MoS_2 hetero-structures were shown to be electrically coupled with each other which lead to enhanced electrocatalytic activity [17]. It was observed that using a graphene layer as support for MoS_2 affects its charge density distribution. The stacking leads to an in-built electric field in the hybrid which results in an excessive negative charge in the hetero-structure. This negative charge improves the hydrogen evolution reaction (HER) electrocatalytic activity. Another report [18] talks about the significant increase in the activity of inert MoS_2 surface by using graphene oxide (GO) as support. The catalytic activity of the MoS_2 basal plane was presented to be affected by the oxygen concentration in the GO. N-doping in the GO substrates further enhanced the catalytic activity giving a ΔG_H value of ~ -0.014 eV.

The effect of substitutional doping in graphene, especially nitrogen [19] (N), is known to tune the electronic spectra enhancing its properties for various applications [20]. While there have been many theoretical [21, 22], and experimental [12, 23], works on graphene:MoS_2 hybrids, effects of N substitution in graphene on the catalytic and

electronic properties have not been investigated yet. Here, we present a detailed theoretical analysis of N-doped graphene:MoS_2 hetero-structures, consisting of different chemical types of N: (i) Graphitic (G), (ii) Pyridinic (Pn), and (iii) Pyrrolic (Pr). This work focusses on the effect of chemical nature of N on the catalytic activity of graphene:MoS_2 hetero-structure. We find that the type of substitutional nitrogen directly affects the electronic structure of the hetero-structure whereas the interlayer distance is about the same in the three cases. The work function (φ) of the hybrid is directly dependent on the type of N present. On doping the graphene layer with graphitic N-atoms, φ of the hetero-structure decreases making it capable of catalysing the reduction of H^+ thus producing H_2, while it increases when doped with Pn N-atoms as well as Pr N-atoms. The use of 1H-MoS_2 as support results in increased H_2O adsorption therein improving the catalytic activity. Pr N-doped graphene:MoS_2 hetero-structure turns out to a direct narrow band gap semiconductor with a band gap value (E_g) of ~266 meV. The results are also compared to the pristine graphene:MoS_2 hetero-structure.

3.2 Computational Details

Our first-principles calculations are based on density functional theory (DFT) as implemented in the Quantum ESPRESSO code [24], employing a plane-wave basis set and an ultrasoft pseudopotential [25] to represent the interaction between ionic cores and valence electrons. We adopt the exchange-correlation functional of Perdew-Burke-Ernzerhof (PBE) [26] within a generalised gradient approximation (GGA). We smear the occupation numbers of electronic states with Fermi–Dirac distribution and a smearing width (k_BT) of 0.04 eV. van der Waals (vdW) interactions are included using Grimme scheme [27]. An energy cutoff of 40 Ry on the plane-wave basis is used in representation of Kohn-Sham wave functions, and 320 Ry to represent the charge density. Structures are determined through minimization of energy until the Hellmann-Feynman forces on each atom are smaller than 0.03 eV/Å in magnitude. We sampled Brillouin-zone integrations on uniform grid of 5x5x1 K-points. The projected density of states for the hetero-structures was obtained from a much denser (11x11x1) K-point mesh. Calculated lattice constants of both 1H-MoS_2 (a_{MoS_2} = 3.19 Å) and graphene monolayer (a_{Gr} = 2.46 Å) are in good agreement with the respective experimental values ($a^{\circ}_{MoS_2}$ = 3.16 Å) [28]

and (a°_{Gr} = 2.46 Å) [29] respectively. Hetero-structures between MoS_2 and N-substituted graphene are modelled using Virtual NanoLab (VNL) [30] (see Fig 3.1). Each supercell comprises of 5x5 unit cells graphene stacked over 4x4 unit cells of MoS_2 amounting to a small lattice mismatch (~2.7%). A vacuum layer of 15 Å is introduced parallel to the interface separating adjacent periodic images of the hetero-structure.

3.3 Constructing the Hetero-structures

To construct the hetero-structures we place a 5x5 graphene sheet on a 4x4 1H-MoS_2 where a C atom of graphene is placed on top of one of the Mo atoms of the MoS_2 sheet. It was previously shown that relative in-plane position of graphene over the MoS_2

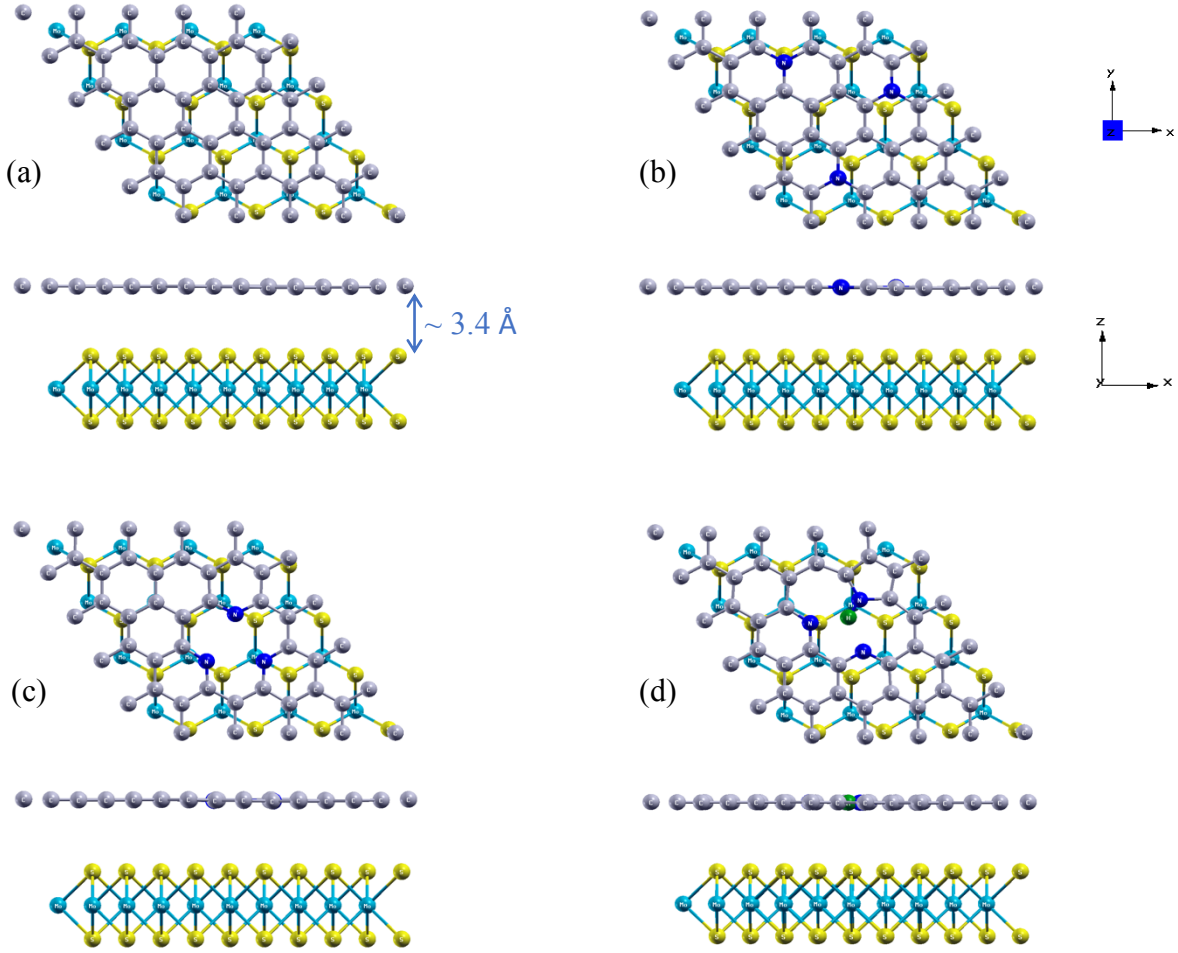

Figure 3.1 Top and side view of constructed hetero-structure, (a) Pristine graphene:MoS_2, (b) graphitic N-graphene:MoS_2, (c) pyridinic N-graphene: MoS_2, and (d) pyrrolic N-graphene:MoS_2. Grey, blue, cyan, yellow and green spheres represent carbon, nitrogen, molybdenum, sulfur and hydrogen atoms respectively.

monolayer affects neither the energetics, nor the electronic properties of the system [21]. To determine the properties of N-graphene:MoS_2 hetero-structure we employ three defect configurations as mentioned above. The "graphitic" N corresponds to simply replacing C atoms by N atoms in the graphene layer. The "pyridinic" and "pyrrolic" N, refer to the N atoms which contribute one and two electrons respectively to the $\boldsymbol{\pi}$ conjugated system [31]. The G N-graphene:MoS_2 (Fig 3.1b) is obtained by replacing 6% C atoms of the graphene sheet with N atoms. The substituted N atoms are placed at relatively far positions so as to weaken the interaction between the N atoms. Pn N-graphene:MoS_2 (Fig 3.1c) comprises of three pyridine rings created by introducing 6% N-substitution and 2% vacancies in the graphene sheet creating the pyridine-like environment for N atoms. The Pr N-graphene:MoS_2 (Fig 3.1d) structure is obtained in the same manner as the Pn N-graphene:MoS_2, however, two N atoms induce pyridine like nature and one N atom forms a 5-membered pyrrole ring. A hydrogen atom (H) bonded to the N atom is introduced into the system in order to satisfy the valency of pyrrolic N atom.

3.4 Adhesion between the two Monolayers

The optimum interlayer spacing between the two monolayers is calculated by evaluating binding energy (E_b) between the graphene and MoS_2 using the following expression:

$$\boldsymbol{E_b = \frac{\left[E_{N-Graphene:MoS_2} - \left(E_{N-Graphene} + E_{MoS_2}\right)\right]}{N_C}}$$

where $E_{N-Graphene:MoS_2}$, E_{MoS_2}, $E_{N-graphene}$ are the energies of the hetero-structure, isolated 1H-MoS_2 (4x4), and isolated N-graphene monolayer (5x5), respectively. The obtained values of E_b are plotted as a function of interlayer distance (Fig 3.2).

As evident from the plot, the optimum separation is found to be 3.4 Å which is in reasonable agreement with the previous theoretical reports [21, 31]. $E_b/C-atom$ for the pristine graphene:MoS_2 hetero-structure that we obtained (~ -40 meV) is almost 1.75 times the value available in the literature [21]. The incongruity in the results arises because here we take into account the effect of vdW interactions which were absent in

the previous report [21]. Since vdW interactions are responsible for holding the monolayers together, we believe that it is essential to include their contribution while

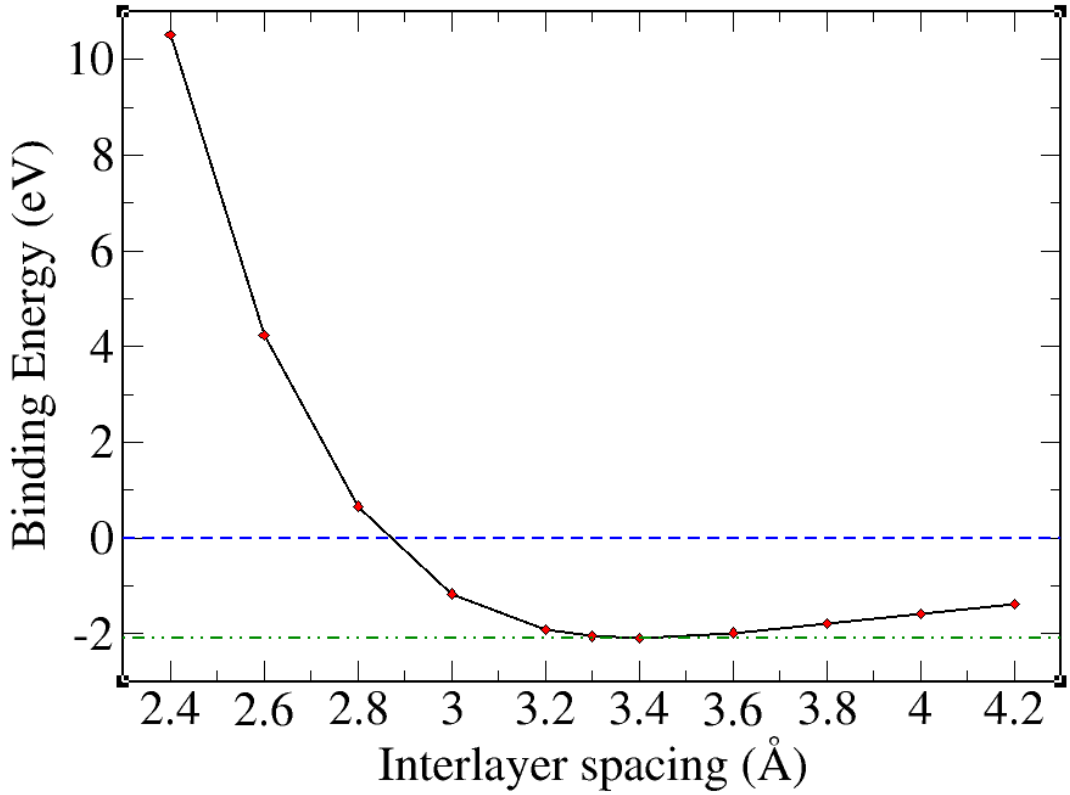

Figure 3.2 Binding energy (E_b) versus interlayer spacing between the two monolayers.

studying such systems. To reaffirm our results, we calculated $E_b/C-atom$ for all the systems without the contribution from vdW forces (Table 3.1). We observe that vdW forces are almost solely responsible for the adhesion between the monolayers. Regardless of the chemical nature, no major change is seen in the $E_b/C-atom$ on doping the graphene sheet with N atoms implying that N-doping does not alter the adhesion of graphene sheet on MoS_2.

Hetero-structure	E_b(meV)/C − atom	
	With vdW	Without vdW
Pristine graphene:MoS_2	-40	-1.5
G N-graphene:MoS_2	-44	-2.9
Pn N-graphene:MoS_2	-43	-3
Pr N-graphene:MoS_2	-43	-3

Table 3.1 Interlayer binding energy calculated (E_b) with and without including vdW interactions.

3.5 Electronic Structure and Projected Density of States

We determine electronic structure and projected density of states (PDoS) of the graphene:MoS_2 hybrids (see Fig 3.4). In case of pristine graphene:MoS_2 hybrid, the band structure is a simple composition of the electronic structure of each component (Fig 3.4a). Graphene retains its linear dispersion and falls in the energy gap of 1H-MoS_2. The orbitals of the C atoms of graphene are at energies between those of Mo and S orbitals as shown in the PDoS of the hetero-structure (Fig 3.4a). Interestingly, the Dirac cone of graphene shows a tiny opening (~ 0.3 meV). Recently, a similar observation was made by Singh et al. [32].

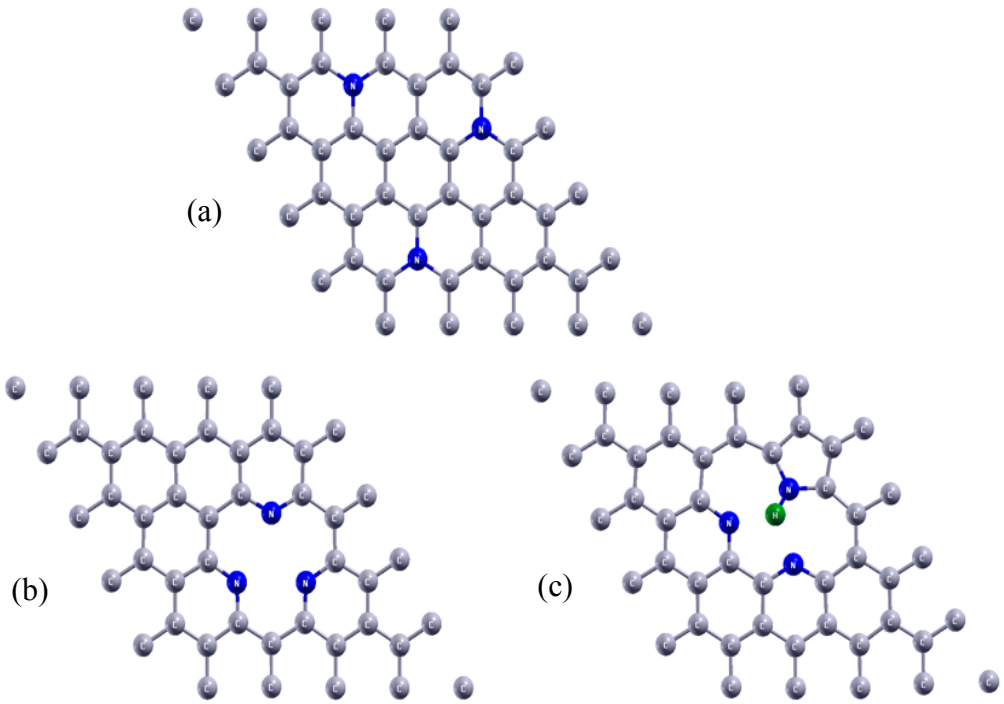

Figure 3.3 Schematic representation of (a) graphitic N-graphene:MoS_2, (b) pyridinic N-graphene:MoS_2, and (c) pyrrolic N-graphene:MoS_2. Carbon, nitrogen and hydrogen atoms are represented by grey, blue and green spheres respectively.

The inclusion of nitrogen atoms of different chemical nature changes the electronic structure of the graphene:MoS_2 hetero-structure remarkably. Replacing three C atoms of graphene with N atoms renders a graphitic N-doped configuration (Fig 3.4a). These N-

dopants furnish the system with extra electrons that couple with the neighbouring C atoms causing the Dirac point to shift up, hence imparting an n-doped character to the system. The linear dispersion nature of graphene bands is not present anymore and a small gap (~ 0.1 eV) opens up at the Dirac point. The bands at the Dirac point are parabolic in nature which is seen throughout the N-doped hetero-structures irrespective of the chemical identity. States arising due to N-dopants can be seen just above the Fermi level (E_F) in the PDoS plot (Fig 3.4b). Graphitic (G) N-doping differs from pyridinic (Pn) N-doping in the sense that in the former, the N atoms are intentionally kept away from each other so as to lessen the N-N interaction (Fig 3.3a). In case of Pn-N doping, three N atoms are placed in close vicinity to each other and a vacancy defect is induced at the centre of these dopants breaking the $\boldsymbol{\pi}$ conjugation and creating a pyridine ring like environment (Fig 3.3b). The Pn-N defect causes an opposite effect on the electronic behavior of the graphene:MoS_2 hetero-structure than the one caused by graphitic-N dopants (Fig 3.3c). Of the five valence electrons of nitrogen, two participate in $\boldsymbol{\sigma}$ bond formation with the neighbouring C atoms while one forms $\boldsymbol{\pi}$ state within the pyridine ring. The remaining two electrons form a lone pair as the $\boldsymbol{\pi}$ conjugation is absent due to the vacancy defect present in the centre of the dopants. Presence of lone pair causes a heavy donation of electrons to the valence bands and two new bands arise just below the E_F (see Fig 3.4c). The Pn-N doping shifts the E_F down, giving a p-type doping in the system. The Dirac cone exhibits a parabolic nature with a bigger gap opening (~ 0.48 eV) at the Dirac point than the one seen in the graphitic-N case. Pr N-graphene:MoS_2 hetero-structure consists of two pyridine rings and one pyrrole ring in the graphene sheet (Fig 3.3c). Pyrrolic-N atom uses three of its five valence electrons in $\boldsymbol{\sigma}$ bonding, two with C atoms and one with H atom. The remaining two electrons are delocalized, imparting the pyrrole ring an aromatic nature. Therefore, the pyrrolic-N atom lends two electrons to the $\boldsymbol{\pi}$ conjugated system, hence n-doping the system. Whereas two pyridinic-N present in the sheet cause a p-doping as explained earlier. The opposite effects of the two types of N atoms (Fig 3.4d) cancel each other out resulting in an unaffected E_F and a small band gap opening at the Dirac point. Thus, the Pr N-graphene:MoS_2 hetero-structure turns out to be a direct narrow band gap semiconductor (Fig 3.4d) with a band gap (E_g) of ~266 meV.

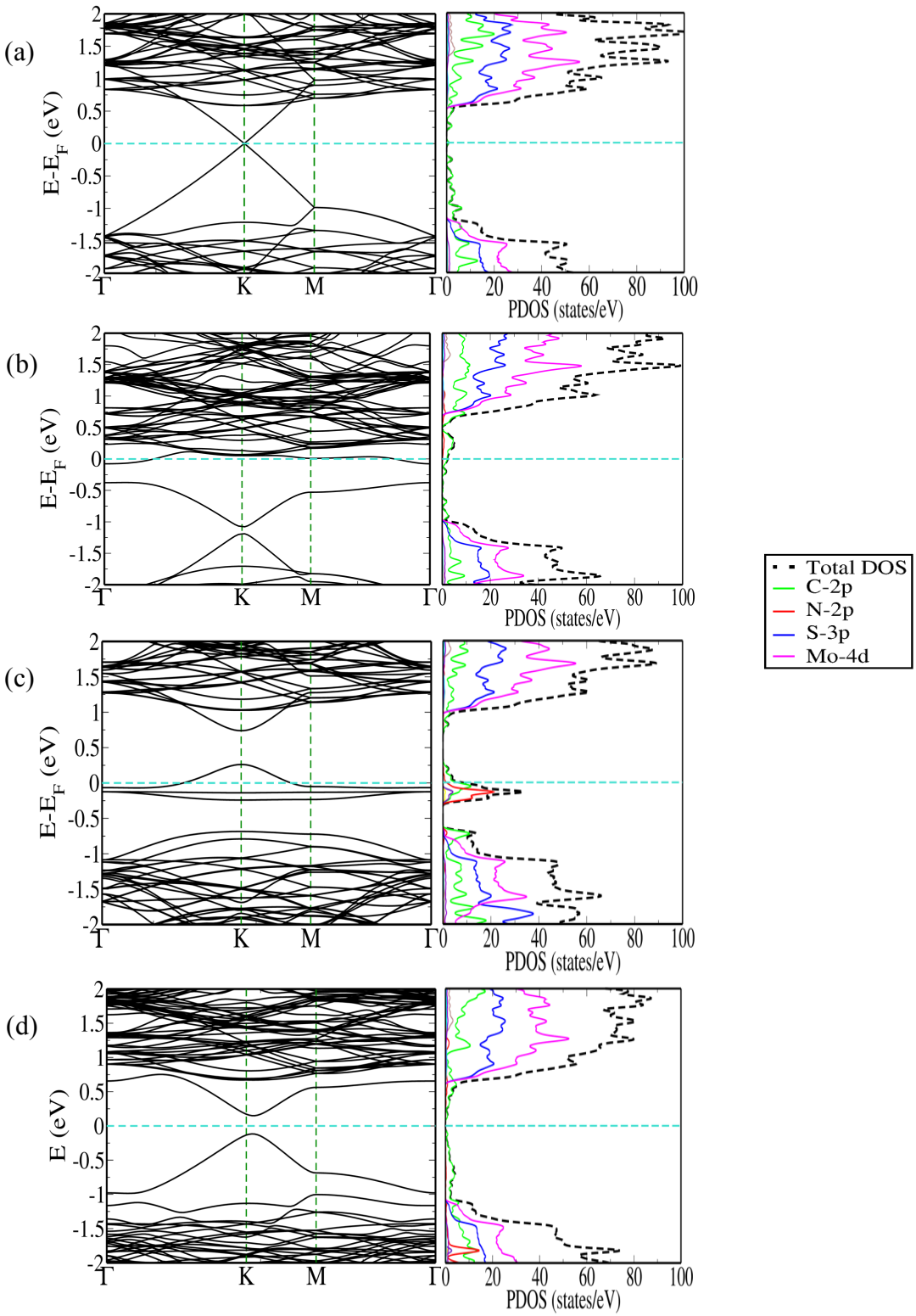

Figure 3.4 Electronic structure and projected density of states (PDoS) of (a) Pristine graphene:MoS_2, (b) graphitic N-graphene:MoS_2, (c) pyridinic N-graphene:MoS_2, and (d) pyrrolic N-graphene:MoS_2. We note an overlapping electronic structure of graphene and MoS_2 (a), n-type character in graphitic N-doped graphene:MoS_2 (b), defect bands of N and p-type character in the valence band of graphene (c), and a gap opened up in graphene bands in (d).

3.6 Work Function

Work function (φ) is defined as the minimum amount of work done required to remove an electron from the interior of a material to vacuum. The reactivity of the a catalyst can be determined by its work function. The following expression is used to calculate work function of a metal:

$$\varphi = E_{vac} - E_F$$

where E_{vac} is the vacuum potential. The above-mentioned formula is used to calculate the φ values for the pristine graphene:MoS_2, G N-graphene:MoS_2, and Pn N-graphene:MoS_2 since they have nonzero electronic density of states at E_F. To calculate the φ for Pr N-graphene:MoS_2, we use the following expression:

$$\varphi = E_{vac} - E_{VBM}$$

where E_{VBM} is the energy of valence band maxima. We align the band edge energies on the standard hydrogen electrode (SHE) potential scale in order to benchmark out results (see Fig 3.4). On aligning the band edges on the SHE energy scale we observe that doping graphene with G N-atoms, decreases the φ of the hetero-structure, while Pn and Pr N-atoms increase the φ (see Table 3.2).

Hetero-structure	Work Function
Pristine graphene:MoS_2	4.5
G N-graphene:MoS_2	3.8
Pn N-graphene:MoS_2	4.97
Pr N-graphene:MoS_2	4.7

Table 3.2 Calculated work function values of the hetero-structures.

The hydrogen reduction potential (E_H°) falls just below the E_F (Fig 3.5) in case of G N-graphene:MoS_2, suggesting it to be a viable catalyst for HER. Pristine graphene:MoS_2, Pn and Pr N-graphene:MoS_2 hetero-structures turn out to be photocatalysts for HER (Fig 3.5). However, Pn N-graphene:MoS_2 has abundant electrons available at the E_F (Fig 3.4c) proposing it to be a better photocatalyst than the other two.

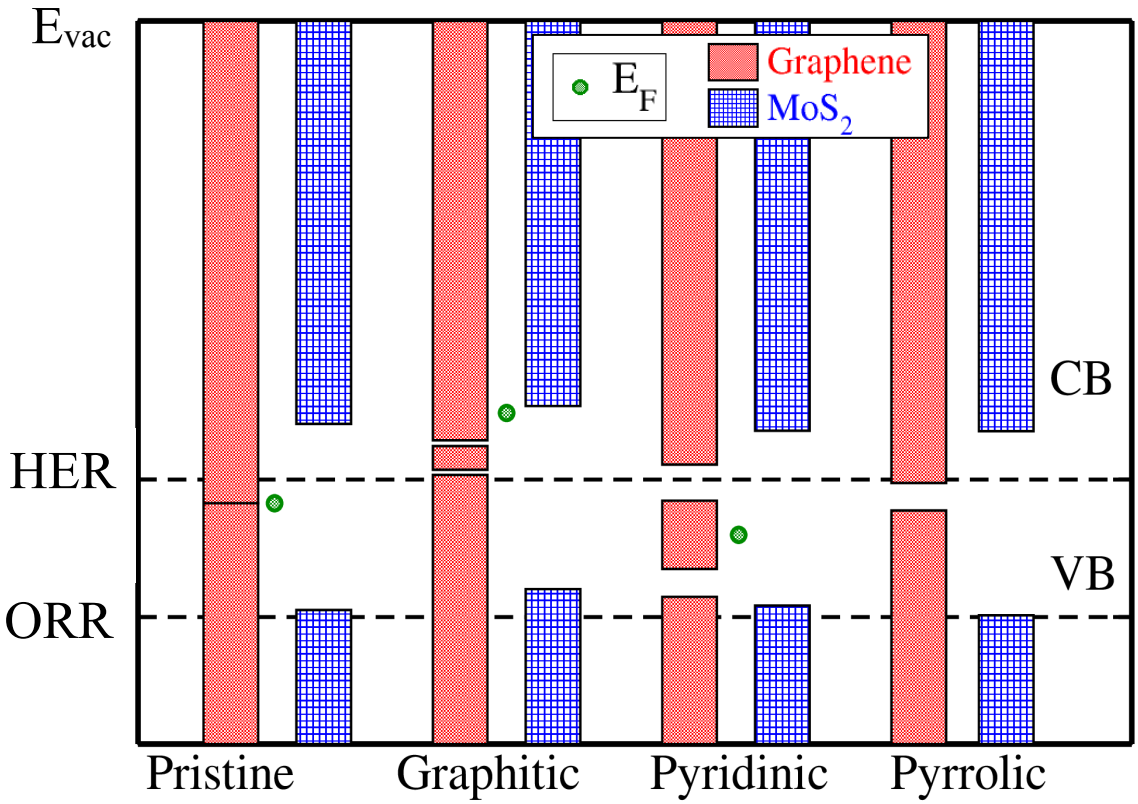

Figure 3.5 Alignment of electronic bands of graphene (red) and MoS_2 (blue) with respect to standard hydrogen electrode (HER) and oxygen reduction potential (ORR) and vacuum. Green circles denote the Fermi energy.

3.7 Catalysis of HER

In order to test the catalytic activity of the hetero-structures, we simulated the adsorption of H-atom, H_2O molecule and OH at various adsorption sites for all the four hetero-structures. Initial distance ($d_{initial}$) between the adsorbate and surface is taken as:

$$d_{initial} = (r_A + r_B)\,[1 + 0.2]$$

where, r_A and r_B are the covalent radii of species A and B respectively. A and B is the atom of surface acting as the adsorption site and atom of the adsorbate placed directly over A, respectively. We evaluate the interaction strength between the adsorbate and the surface using the following expression:

$$\Delta E_{ads} = E_{complex} - (E_{heterostructure} + E_{adsorbate})$$

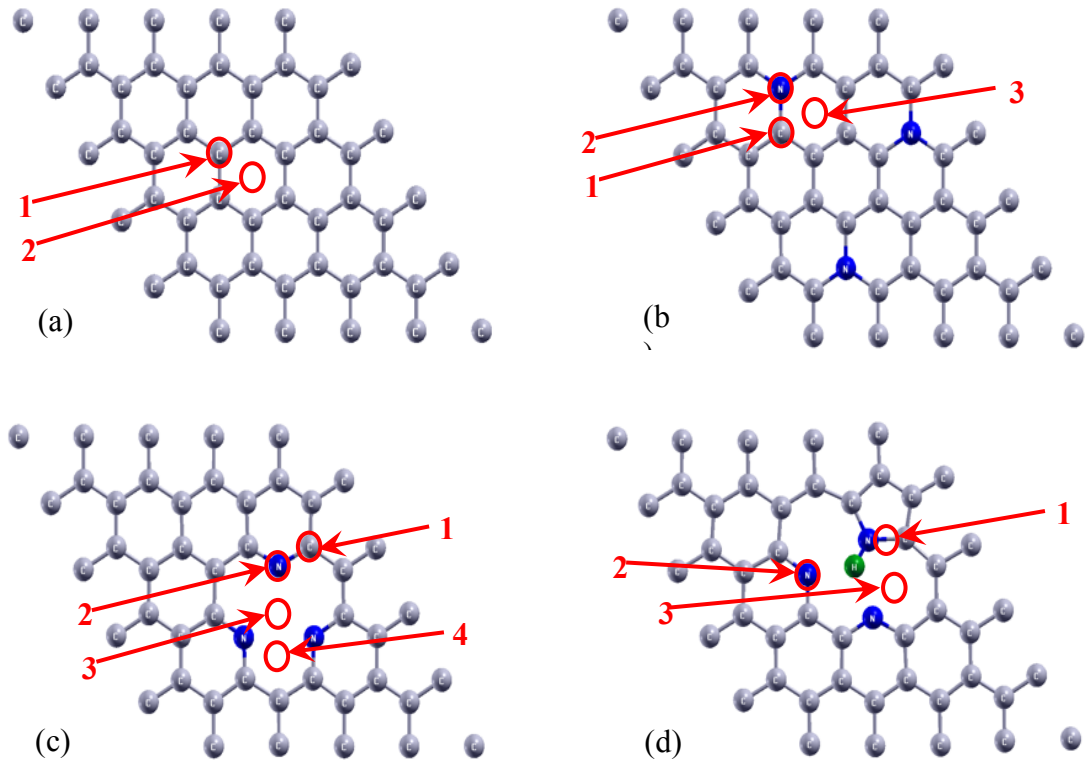

Figure 3.6 Selected adsorption sites to study the adhesion of H-atom, OH and H_2O molecule for (a) Pristine graphene:MoS_2, (b) graphitic N-graphene:MoS_2, (c) pyridinic N-graphene:MoS_2, and (d) pyrrolic N-graphene:MoS_2 hetero-structures. Carbon, nitrogen and hydrogen atoms are represented by grey, blue and green spheres respectively.

where, ΔE_{ads} is the adsorption energy and $E_{complex}$, $E_{heterostructure}$, $E_{adsorbate}$ are the total energies of adsorbate-heterostructure complex, (N) graphene:MoS_2 hetero-structures, and isolated adsorbate (H-atom, H_2O and OH) respectively. We take $1/2\, E_{H_2}$ as the energy of an isolated H-atom (E_H). Hydrogen adsorption improves on doping with N in graphene and greatly depends on the chemical nature of the dopant (Table 3.3). The. high ΔE^{H}_{ads} at sites 2, 3 and 4 in the case of Pn N-graphene:MoS_2 hetero-structure are observed because of the vacancy defect present in the graphene ring. H-atom fits into the vacancy bonding to N-atom, thus decreasing the energy of adsorbate-heterostructure complex. In order to understand the effect of MoS_2 on adsorptive nature of the graphene:MoS_2 hetero-structure, we performed one set of adsorption simulations with just N-graphene keeping all other parameters identical. We took Pn N-graphene and simulated the adsorption of H_2O molecule at adsorption sites 1, 2 and 3 (see Fig 3.6c).

We observed a steady decrease in the ΔE_{ads} values as compared to the Pn N-graphene:MoS_2 hetero-structure (Table 3.3).

Gibbs free energy of H adsorption (ΔG_H) has been widely accepted as a descriptor for studying catalysis of HER where a value close to zero is desired [33]. To calculate ΔG_H we use the following expression:

$$\Delta G_H = \Delta E_{ads}^{H} - T\Delta S_H - E_{ZPE}^{H}$$

where ΔE_{ads}^{H} is the H-adsorption energy, $\Delta S_H = {}^{1}/_{2}\, S_{H_2}^{\circ}$, where $S_{H_2}^{\circ}$ is the entropy of H_2 molecule and $E_{ZPE}^{H} = {}^{1}/_{2}\, E_{ZPE}^{H_2}$, where $E_{ZPE}^{H_2}$, is the zero-point energy of isolated H_2 molecule. We take T as room temperature, i.e., 298 K.

Hetero-structure	Adsorption Site	ΔE_{ads}		
		H	**OH**	**H_2O (meV)**
Pristine graphene:MoS_2	1	1.33	-1.41	-134
	2	1.34	-0.87	-424
Graphitic N-graphene:MoS_2	1	0.36	-2.76	-133
	2	1.62	-1.63	-142
	3	0.6	-2.41	-136
Pyridinic N-graphene:MoS_2	1	1.3	-1.4	-170
	2	-2.5	-2.0	-448
	3	-2.5	-2.0	-448
	4	-2.5	-2.4	-440
Pyridinic N-graphene	1	-	-	-162
	2	-	-	-192
	3	-	-	171
Pyrrolic N-graphene:MoS_2	1	0.6	-1.8	-170
	2	-0.16	-0.8	-208
	3	-0.14	-0.85	-82

Table 3.3 Adsorption energy ΔE_{ads} for pristine and N-doped graphene:MoS_2 hetero-structures at various adsorption sites.

Graphitic N-graphene:MoS_2 hetero-structure gives the lowest ΔG_H of ($\sim 0.025\ eV$) at adsorption site 1 (see Fig. 3.7). Thus, graphitic N-dopants reduce the work function as well as the ΔG_H making the hetero-structure an excellent candidate for catalysing the evolution of hydrogen.

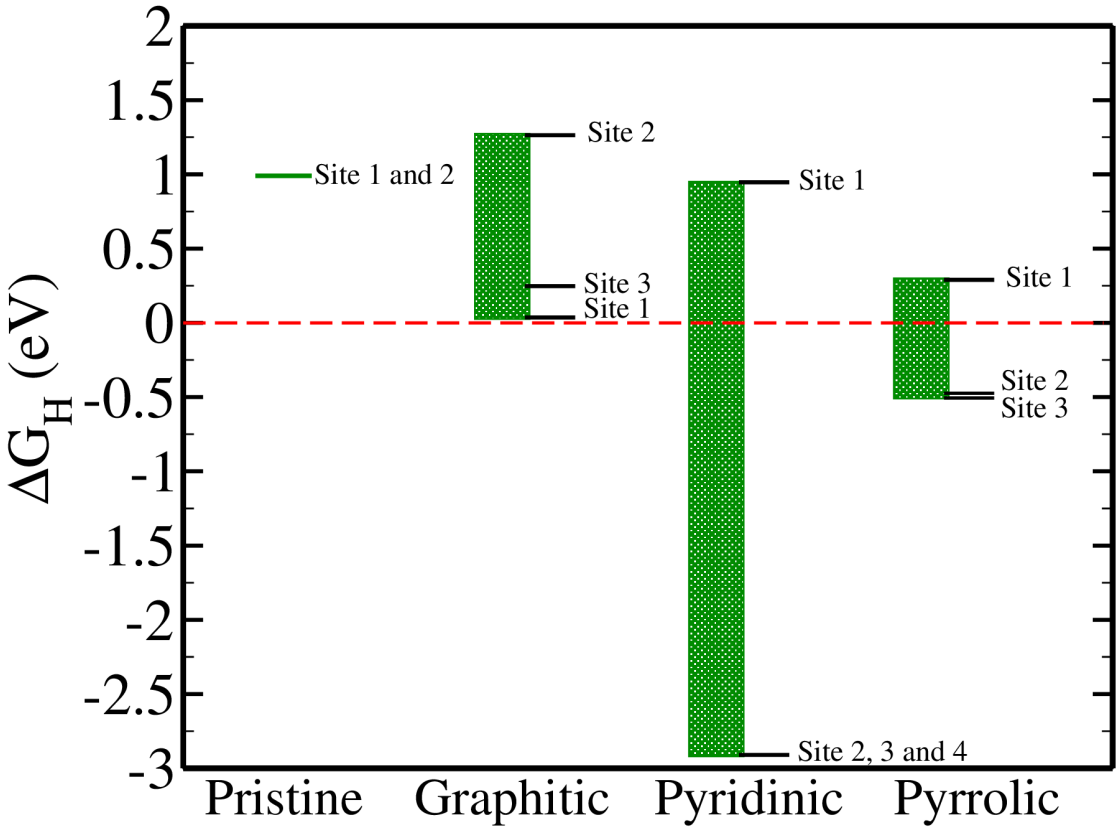

Figure 3.7 Gibbs free energies of H adsorption calculated for pristine and N-doped graphene:MoS_2 hetero-structures at various adsorption

3.8 Conclusions

Using first-principles calculations we determine the impact of N-dopants on the adhesive properties of graphene:MoS_2 van der Waals hetero-structures. It is found that doping with N atoms (G, Pn, Pr) does not alter the adhesion between the two monolayers showing a binding energy of -40 (-44, -43) meV per C atom for the pristine (doped) system(s). Also, the synergy between the monolayers is predominantly governed by van der Waals

interactions. The interlayer spacing is observed to be constant for all the four systems and has a value of ~3.4 Å.

The pristine graphene:MoS_2 hetero-structure shows a negligible shifting of the Dirac cone above the E_F. Also, a minute opening of the bands is obtained at the Dirac point (~0.3 meV). The electronic properties of the hetero-structure are however strongly influenced by the chemical nature of the N-atoms. The graphene:MoS_2 hybrid experiences an n-type doping due to the G and Pr N-dopants as these N-atoms contribute one and two electrons, respectively, to the $\boldsymbol{\pi}$ conjugated system of the graphene ring. The Pn N-dopants on the other hand p-dope the system as the $\boldsymbol{\pi}$ conjugation is absent due to the vacancy defect in the graphene layer. Also, the Dirac cone loses its linear dispersion nature and the bands now exhibit a parabolic behavior which is seen throughout the N-doped hetero-structures irrespective of the chemical identity. Thus, the G N-graphene:MoS_2 behaves like an n-type semiconductor and small gap (~ 0.1 eV) opens up at the Dirac point. The Pn N-graphene:MoS_2 hybrid is observed to behave like a p-doped semiconductor with a bigger gap opening (~ 0.48 eV) at the Dirac point. The Pr N-graphene:MoS_2 hetero-structure has a competitive contribution from the two types of N dopants present in it. The two Pn N-atoms make the system electron deficient whereas the Pr N-atom, furnishes the system with two electrons. As a result, the Pr N-graphene:MoS_2 hetero-structure behaves like a direct narrow band gap semiconductor and exhibits a E_g of ~266 meV. Doping the hetero-structure with G N-atoms reduces its work function making it viable for reducing H^+. Calculated ΔG_H indicate that graphitic N-graphene:MoS_2 hetero-structure ($\Delta G_H \sim 0.025\ eV$) has potential as a catalyst for HER. We also show that using 1H-MoS_2 as support increases the adhesion between the adsorbate and the hetero-structure. These results offer useful insights for deciphering and enhancing catalytic activity of vdW hetero-structures.

Bibliography

[1] K. S. Novoselov, A. K. Geim, S. V. Morozov, D. Jiang, Y. Zhang, S. V. Dubonos, I. V. Grigorieva, A. A. Firsov, *Science* **306**, 5696 (2004).

[2] Jian-Hao Chen, Chaun Jang, Shudong Xiao, Masa Ishigami and Michael S. Fuhrer, *Nature Nanotechnology* **3**, 206 - 209 (2008).

[3] Alexander A. Balandin, Suchismita Ghosh, Wenzhong Bao, Irene Calizo, Desalegne Teweldebrhan, Feng Miao, and Chun Ning Lau, *Nano Lett.* **8**, 902–907 (2008).

[4] R. R. Nair, P. Blake, A. N. Grigorenko, K. S. Novoselov, T. J. Booth, T. Stauber, N. M. R. Peres, A. K. Geim, *Science* **320**, 1308–1308 (2008).

[5] Changgu Lee, Xiaoding Wei, Jeffrey W. Kysar, James Hone, *Science* **321**, 385–388 (2008).

[6] MD Stoller, S Park, Y Zhu, J An, RS Ruoff, *Nano Lett.* **8**, 3498–3502 (2008).

[7] K. S. Novoselov, D. Jiang, F. Schedin, T. Booth, V. Khotkevich, S. Morozov, A. Geim, *Proc. Natl. Acad. Sci. U.S.A.* **102**, 10451− 10453 (2005).

[8] Y. P. Venkata Subbaiah, K. J. Saji, A. Tiwari, *Adv. Funct. Mater.* 2016, **26**, 2046-2069.

[9] Kin Fai Mak, Changgu Lee, James Hone, Jie Shan, and Tony F. Heinz, *Phys. Rev, Lett.* **105**, 136805 (2010).

[10] AK. Geim and I. V. Grigorieva, *Nature* **499**, 419-425 (2013).

[11] K. S. Novoselov, A. Mishchenko, A. Caravalho, A. H. Castro Neto, *Science* **353**, 6298 (2016).

[12] Ravi K. Biroju, Deya Das, Rahul Sharma, Shubhadeep Pal, Larionette P. L. Mawlong, Kapil Bhorkar, P. K. Giri, Abhishek K. Singh,and Tharangattu N. Narayanan, *ACS Energy Lett.* **2**, 1355−1361 (2017).

[13] Linfeng Wang, Xiang Zhou, Tianbao Ma, Dameng Liu, Lei Gao, Xin Li, Jun Zhang, Yuanzhong Hu, Hui Wang, Yadong Dai, Jianbin Luo, *Nanoscale* 2017.

[14] Sushant Kumar Behera, Pritam Deb, and Arghya Ghosh, *ChemistrySelect* **2**, 3657 – 3667 (2017).

[15] Horacio Coy Diaz, José Avila, Chaoyu Chen, Rafik Addou, Maria C. Asensio, and Matthias Batzill, *Nano Lett.* 1**5,** 1135−1140 (2015).

[16] Kun Chang and Weixiang Chen, *Chem. Commun.* **47**, 4252–4254 (2011).

[17] Honglin Li, Ke Yu, Chao Li, Zheng Tang, Bangjun Guo, Xiang Lei, Hao Fu & Ziqiang Zhu, *Sci Rep* **5**, Article number: 18730 (2015).

[18] Shaobin Tang, Weihua Wu, Shiyong Zhang, Dongnai Ye, Ping Zhong, Xiaokang Li, Liangxian Liu and Ya-Fei Li, *Phys.Chem.Chem.Phys.* **20**,1861-1871 (2018).

[19] L. S. Panchakarla, K. S. Subrahmanyam, S. K. Saha, A. Govindaraj, H. R. Krishnamurthy, U. V. Waghmare, and C. N. R. Rao, *Adv. Mater.* **21**, 4726-4730 (2009).

[20] Congcong Ma, Xiaohong Shao and Dapeng Cao, *J. Mater. Chem.* **22**, 8911 (2011).

[21] Yandong Ma, Ying Dai, Meng Guo, Chengwang Niu and Baibiao Huang, *Nanoscale* **3**, 3883 (2011).

[22] Xingen Liu and Zhongyao Li, *J. Phys. Chem. Lett.* **6**, 3269−3275 (2015).

[23] Ravi K Biroju, Shubhadeep Pal, Rahul Sharma, P K Giri and Tharangattu N Narayanan, *Nanotechnology* **28**, 085101 (2017).

[24] P. Giannozzi *et al.*, *J. Phys. Condens. Matter* **21**, 395502 (2009); www.quantum-espresso.org.

[25] D. Vanderbilt, Soft self-consistent pseudopotentials in a generalized eigenvalue formalism, *Phys. Rev. B* **41**, 7892 (1990).

[26] J. P. Perdew, K. Burke, and M. Ernzerhof, *Phys. Rev. Lett.* **77**, 3865 (1996).

[27] S. Grimme, *J. Comput. Chem.* **27**, 1787–1799 (2006).

[28] K. D. Bronsemja, L. De Boer, and F. Jellinek, *Z. anorg. allg. Chem.* **540/541** (1986).

[29] H. W. King, CRC Handbook of Chemistry and Physics **83**, 19 (2002).

[30] Virtual NanoLab version 2016.4, QuantumWise A/S (www.quantumwise.com).

[31] Dacheng Wei, Yunqi Liu, Yu Wang, Hongliang Zhang, Liping Huang, and Gui Yu, *Nano Lett.* **9**, 1752-1758 (2009).

[32] Sobhit Singh, Camilo Espejo, Aldo H. Romero, arXiv:1802.03919 [cond-mat.mtrl-sci]

[33] Hinnemann, B.; Moses, P. G.; Bonde, J.; Jørgensen, K. P.; Nielsen, J. H.; Horch, S.; Chorkendorff, I.; Nørskov, J. K., *J. Am. Chem. Soc.* **127**, 5308−5309 (2005).

Chapter 4

Co-Mo-P alloy-based Catalyst for superior Alkaline HER: A first-principles study

4.1 Introduction

Hydrogen (H_2) is presently the best potential replacement available for the conventional energy sources due to its minimal ecological footprints. Currently, the main source of energy, fossil fuels have led to global climate change are progressing towards their inevitable exhaustion. In this regard, mass production of H_2 molecule in a cost-effective manner is highly desirable. The most explored method of H_2 production is by electrochemical and photoelectrochemical splitting of water. Metals belonging to the platinum group are known to be the most efficient at executing the hydrogen evolution reaction (HER) [1], one of the half-cell reactions involved in water splitting. At present, the best available electrocatalyst, platinum, is often used as the standard to compare the performance of other catalysts. However, the expense associated with platinum group metals as well as their low abundance minimize their widespread application as electrocatalysts for HER. Hence, there is a global need to discover new cost-effective materials and optimize their ability to drive the HER.

Water splitting consists of two half-cell reactions, HER which corresponds to reduction of two protons to evolve H_2, and oxygen evolution reaction (OER) in which a water molecule gets oxidized to give out oxygen (O_2). In order to achieve HER at an industrial scale, one medium should be able to carry out both HER and OER. Since many non-expensive OER catalysts operate in an alkaline medium, it is preferred to find catalysts which execute HER in the same medium efficiently. Here we discuss a nonprecious metal-based catalyst for alkaline constituting cobalt (Co), molybdenum (Mo) and phosphorus (P) within the framework of density functional theory. We show that synergy between Mo and P effectively tunes the energetics of the HER reaction intermediates giving rise to the excellent catalytic activity of Co-Mo-P alloy in alkaline medium.

4.2 Computational Details

Our first-principles calculations are based on density functional theory (DFT) as implemented in the Quantum ESPRESSO code [2], employing plane-wave basis and ultrasoft pseudopotentials [3] to represent the interaction between ionic cores and valence electrons. We adopt the exchange-correlation energy functional of Perdew-Burke-Ernzerhof (PBE) [4] obtained within a generalised gradient approximation (GGA). We

smear the occupation numbers of electronic states with Fermi–Dirac distribution and a smearing width (k_BT) of 0.04 eV. An energy cutoff of 40 Ry is used to truncate the plane-wave basis used in representation of Kohn-Sham wave functions, and 320 Ry to represent the charge density. Structures are determined through minimization of energy until the Hellmann-Feynman forces on each atom are smaller than 0.03 eV/Å in magnitude. Two supercells for Co-Mo-P alloy with different compositions are constructed (i) $Co_{28}Mo_4P_4$ and (ii) $Co_{12}Mo_2P_2$ (Fig 4.2). We sampled Brillouin-zone integrations on uniform grids of 5x5x1 k-points for $Co_{28}Mo_4P_4$ and 3x3x3 k-points for $Co_{12}Mo_2P_2$. Calculated lattice constants of Co (a_{Co} = 2.47 Å, c_{Co}= 3.93 Å) are in good agreement with the experimental values (a°_{Co} = 2.5 Å, c°_{Co}= 4.07 Å) [5].

4.3 Generating Co-Mo-P Alloy

Cobalt exists in a hexagonal closed packed (hcp) structure having $P6_3/mmc$ space group at room temperature. The bulk unit cell consists of two basis atoms. To generate the Co-Mo-P alloy we take a cobalt supercell (3x3x1) and dope molybdenum and phosphorus in molar ratio Co:Mo:P ~ 78:11:11. We substitute molybdenum and phosphorus in 3x3x1 bulk cobalt matrix in varied configurations (Mo-P domain(s), isolated Mo and P atom(s)) and compute the energetically most stable structure (see Fig 4.1). We consider the following doping arrangements:

(i) **$Co_{14}Mo_2P_2$_Bulk_1:** Two Mo-P domains

(ii) **$Co_{14}Mo_2P_2$_Bulk_2:** One Mo-P domain and one isolated Mo and P atoms each.

(iii) **$Co_{14}Mo_2P_2$_Bulk_3:** One Mo-Mo domain and two isolated P atoms.

(iv) **$Co_{14}Mo_2P_2$_Bulk_4:** Two isolated Mo and P atoms each.

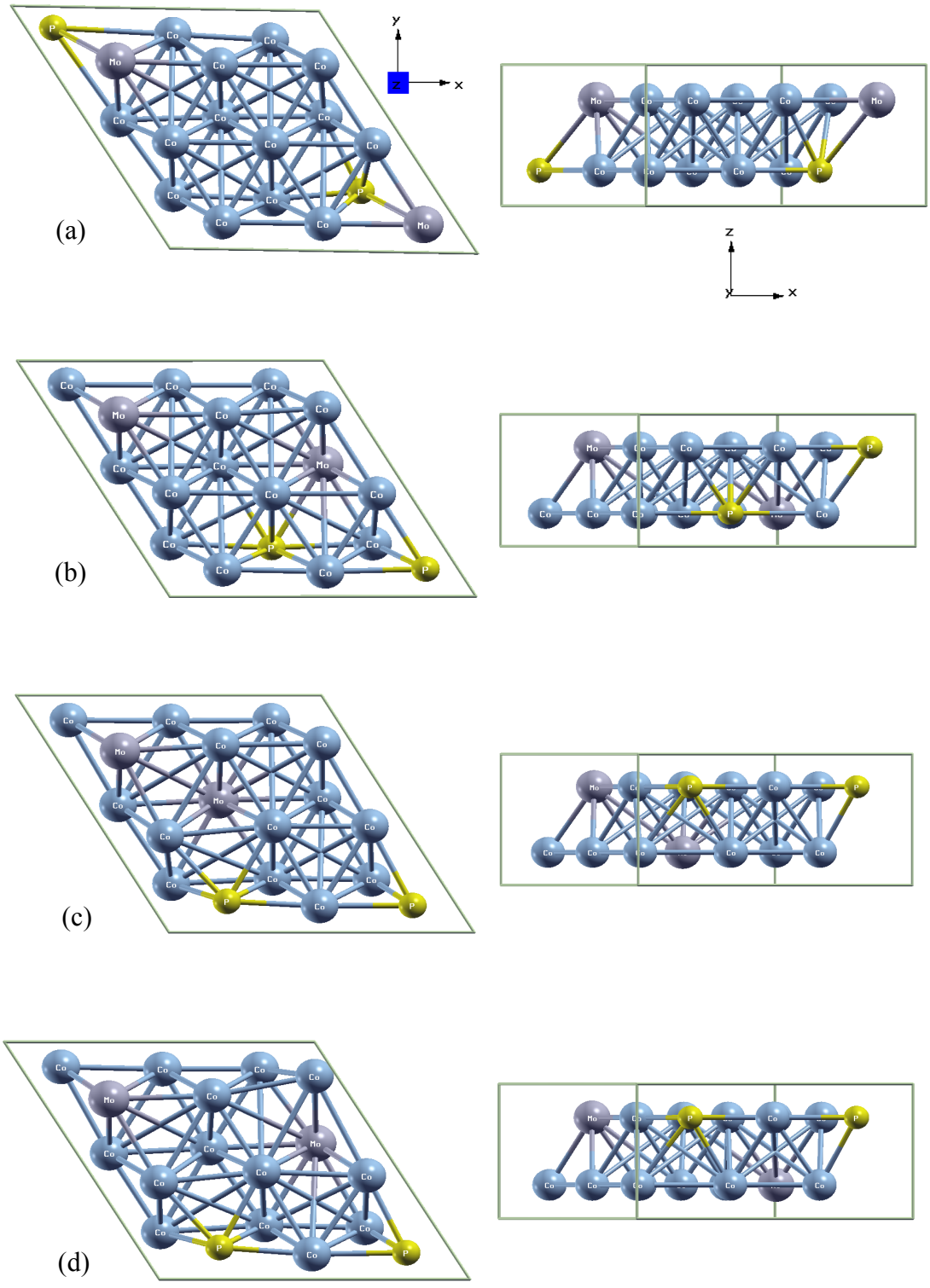

Figure 4.1 Generated $Co_{12}Mo_2P_2$ structures: (a) $Co_{12}Mo_2P_2$_Bulk_1; (b) $Co_{12}Mo_2P_2$_Bulk_2; (c) $Co_{12}Mo_2P_2$_Bulk_3; (d) $Co_{12}Mo_2P_2$_Bulk_4. Cobalt, molybdenum and phosphorus atoms are denoted as blue, purple and yellow spheres respectively.

We use the following expression to calculate the formation energy of the supercell:

$$E_{form} = E_{Co-Mo-P} - [n_{Co}E_{Co} + n_{Mo}E_{Mo} + n_P E_P]$$

where, $E_{form}, E_{Co-Mo-P}$ is the formation energy and the total energy of the Co-Mo-P supercell. E_{Co}, E_{Mo}, E_P is the energy of one Co, Mo and P atom respectively. n_{Co}, n_{Mo}, n_P are the number of Co, Mo and P atoms in the supercell respectively. We find that $Co_{14}Mo_2P_2$_Bulk_3 has the most negative formation energy (Table 4.1) and hence, is the most stable of the 4 configurations.

	Bulk_1	Bulk_2	Bulk_3	Bulk_4
E_{form}(eV/supercell)	**-2.9**	**-3.6**	**-3.7**	**-3.58**
$E_{form\_relative}$(eV/supercell)	**0**	**-0.7**	**-0.8**	**-0.68**

Table 4.1 Calculated formation energy values for various doped configurations of $Co_{14}Mo_2P_2$.

Thus, $Co_{14}Mo_2P_2$_Bulk_3, i.e., doping Co matrix with one Mo-Mo domain and two isolated P atoms is taken as the default configuration in further calculations.

4.4 Constructing Amorphous Structures

We simulate two model amorphous structures of Co-Mo-P with different compositions:

1. $Co_{28}Mo_4P_4$: 3x3x2 unit cell with Co:Mo:P ratio ~ 78:11:11.
2. $Co_{12}Mo_2P_2$: 2x2x2 unit cell with Co:Mo:P ratio ~ 75:12.5:12.5.

We employ the expanding lattice method [6] to generate amorphous structures in which we construct a crystalline supercell expanded by 50%, relax it leading to a nanoporous or disordered system. We first construct the Co-Mo-P crystalline supercell (3x3x2 and 2x2x2) of edge length *p*. We increase the cell parameter of the supercell by a factor of $\sqrt[3]{1.5}$, thus increasing its total volume by a factor of 0.5. On relaxing this expanded supercell, we obtain a nanoporous and disordered system for $Co_{28}Mo_4P_4$ and $Co_{12}Mo_2P_2$ respectively (see Fig 4.2).

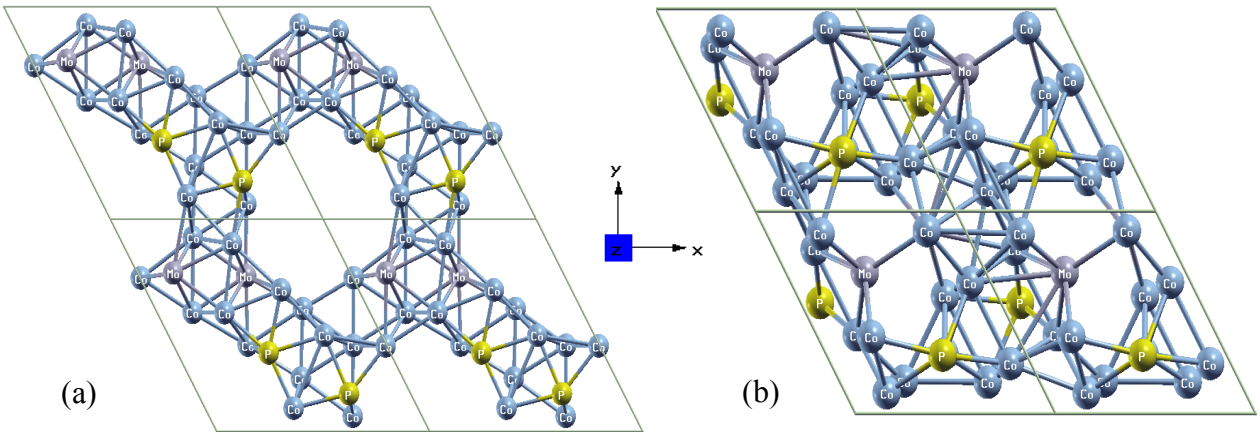

Figure 4.2 (2x2x1) Model amorphous structures of (a) $Co_{28}Mo_4P_4$ and (b) $Co_{12}Mo_2P_2$ obtained using the technique of expanded supercell and relaxation. Cobalt, molybdenum and phosphorus atoms are denoted as blue, purple and yellow spheres respectively.

4.5 Reaction mechanism of Alkaline HER

$$H_2O + M + e^- \longrightarrow M.H_{ads} + OH^- \textbf{ (}\textit{Volmer}\textbf{ step, usual RDS)}$$

$$2M.H_{ads} \longrightarrow H_2 + 2M \textbf{ (}\textit{Tafel}\textbf{ step)}$$

$$H_2O + e^- \longrightarrow H_2 + OH^- \textbf{ (}\textit{Heyrovsky}\textbf{ step)}$$

H_2O molecule serves as the proton source in alkaline solutions. The water molecule dissociates into H atom which gets adsorbed on the metal (M) and an OH^- is released [7].

4.6 Adsorption of H, OH and H_2O

We examine the binding of the reactant (H_2O) and intermediates (H and OH) of alkaline HER on both supercell a various surface sites. For $Co_{28}Mo_4P_4$, following sites (see Fig 4.3a) are selected to study the adsorption of H, OH and H_2O:

1. In the vicinity of a P-atom.
2. In the vicinity of 2 Co atoms.
3. In the vicinity of 1 Mo-atom.
4. In the vicinity of a P and a Co-atom.

Surface sites selected to study the adsorption of H, OH and H_2O on $Co_{12}Mo_2P_2$ are (see Fig 4.3b):

1. In the vicinity of a P-atom.
2. On top of a Co-atom.
3. In the vicinity of 1 Mo and a Co atom.

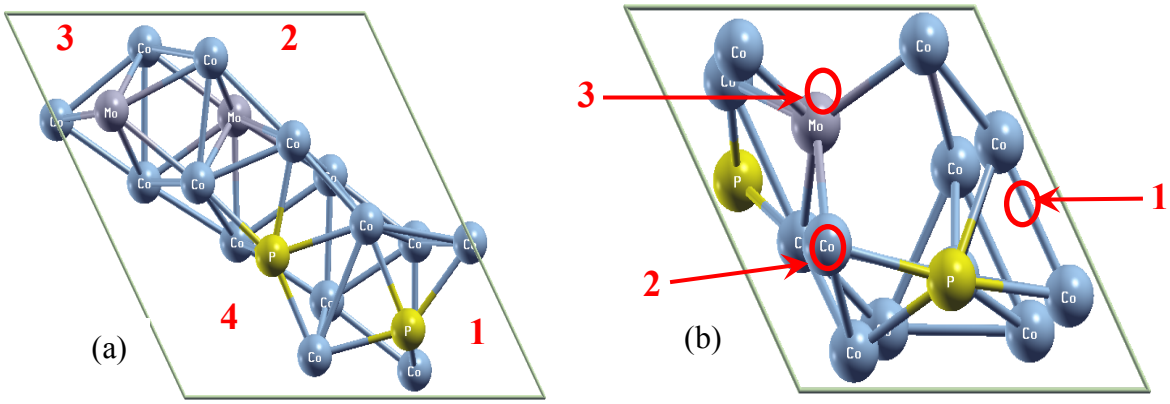

Figure 4.3 The sites of adsorption on (a) $Co_{28}Mo_4P_4$ and (b) $Co_{12}Mo_2P_2$. Cobalt, molybdenum and phosphorus atoms are denoted as blue, purple and yellow spheres respectively.

To calculate adsorption energies, we use the following expression:

$$E_{ads} = E_{system+adsorbate} - \left(E_{system} + E_{adsorbate}\right)$$

where, E_{ads} is the adsorption energy and $E_{system+adsorbate}, E_{system}$ *and* $E_{adsorbate}$ are the total energies of Co-Mo-P+adsorbate complex, Co-Mo-P system, and isolated adsorbate species (H-atom, OH or H_2O molecule respectively). For energy of H-atom, we take $1/2\ E_{H_2}$, where E_{H_2} is the energy of an isolated H_2 molecule.

Upon adsorption of an H_2O molecule at Mo-Co bridging site, we find that the water molecule splits into H* and OH*, where * denotes to an adsorbed entity. The H* attaches to Co, which is what we find as the preferred site of adsorption of H, while the OH binds to a neighbouring Mo-Co bridging site (Fig 4.5a). Thus, we identify Mo-Co site as the active site for splitting H_2O molecule, providing an adsorbed H* atom (*Volmer* step).

Adsorption Site	ΔE_{ads} (eV)					
	$Co_{28}Mo_4P_4$			$Co_{12}Mo_2P_2$		
	H	OH	H_2O	H	OH	H_2O
1	**-3.19**	**-6.62**	**-2.57**	**-2.4**	**-5.22**	**-1.98**
2	**-2.85**	**-6.04**	**-2.26**	**-1.96**	**-5.75**	**-1.36**
3	**-3.17**	**-6.72**	**-2.5**	**-2.5**	**-5.8**	**-2.5**
4	**-3.21**	**-5.76**	**-2.25**	**-**	**-**	**-**

Table 4.2 Adsorption energies of H, OH and H_2O molecule at various adsorption sites shown in Fig 4.3.

Our simulations of adsorption at various sites show that O-atom of both OH and H_2O binds very strongly to either Mo or Co atomic sites (Table 4.2). To understand the role of phosphorus in OH adsorption, if any, we compared its adsorption on (A) $Co_{14}Mo_2$ and (B) $Co_{14}P_2$ (Fig 4.4).

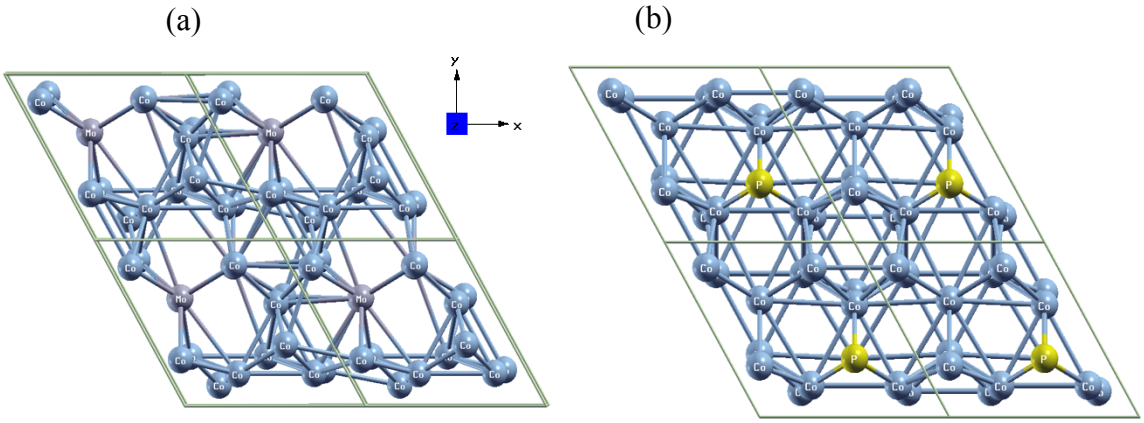

Figure 4.4 Model structures of (a) $Co_{14}Mo_2$ and (b) $Co_{14}P_4$ obtained with 2x2x1 supercell. Cobalt, molybdenum and phosphorus atoms are represented with blue, purple and yellow spheres respectively.

We find that the energies of adsorption of OH ($\Delta E_{ads(OH)}$) and H_2O ($\Delta E_{ads(H_2O)}$) on $Co_{14}P_2$ are higher than those on $Co_{14}Mo_2$ (Table 4.3). P being an electronegative element, ionizes the metal atom in its vicinity, inducing a positive charge (Fig 4.5b). This electron deficient metal site is attractive for adsorption of an electron-rich species (like OH and

H_2O). Thus, $|E_{ads(H_2O)}|$ and $|E_{ads(OH)}|$ are much higher in $Co_{14}P_2$ than $Co_{14}Mo_2$, with intermediate strength of adsorption on $Co_{12}Mo_2P_2$ (Fig 4.5a).

Adsorbate	ΔE_{ads} (eV)		
	$Co_{14}Mo_2$	**$Co_{12}Mo_2P_2$**	**$Co_{14}P_2$**
H	**-0.63**	**-2.4**	**-4.77**
OH	**-4.32**	**-5.22**	**-8.5**
H_2O	**-0.36**	**-1.98**	**-4.3**

Table 4.3 Adsorption energies of H, OH and H_2O molecule at the adsorption site **1** of $Co_{14}Mo_2$, $Co_{12}Mo_2P_2$ and $Co_{14}P_2$.

Thus, phosphorus site is key to facilitating the *Heyrovsky* step. Analysis of the projected density of states (PDoS) of OH*$Co_{12}Mo_2P_2$ and H_2O*$Co_{12}Mo_2P_2$ (see Fig. 3c) shows that the highest occupied molecular orbital (HOMO) of the adsorbates (OH and H_2O) is close to the bottom of the d-band of the catalyst. As the HOMO of OH is degenerate and partially occupied, charge transfers from the catalyst metal to OH. In addition, the peak associated with its HOMO splits and broadens due to covalent interaction with orbitals of Mo and P, whose peaks are also close to that of the HOMO of OH. The latter is weak when there is no P in the system (e.g. $Co_{14}Mo_2$). As the HOMO of H_2O is fully occupied and lower in energy relative to the frontier bands of the catalyst, their interaction is weaker, and associated HOMO peaks are sharper. In comparison with H-adsorption on $Co_{12}Mo_2P_2$, H binds much more strongly to $Co_{14}P_2$ while it binds more weakly to $Co_{14}Mo_2$ (see Fig 4.5). Thus, Mo in the Co-Mo-P alloy weakens H-binding facilitating the release of H_2 molecule (*Tafel* step). The synergy between Mo and P gives ride to the excellent catalytic activity of Co-Mo-P alloy in alkaline HER. As pointed out here, the alloy effectuates the steps of HER with each atom playing an important role.

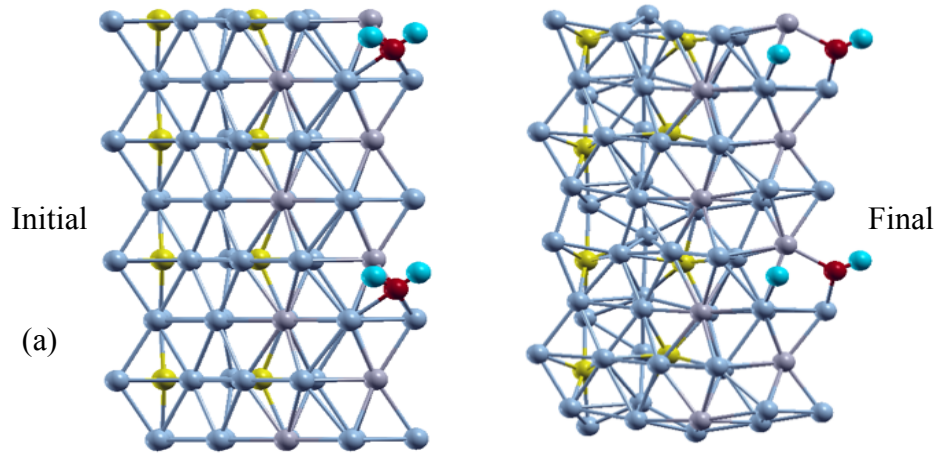
Initial
Final
(a)

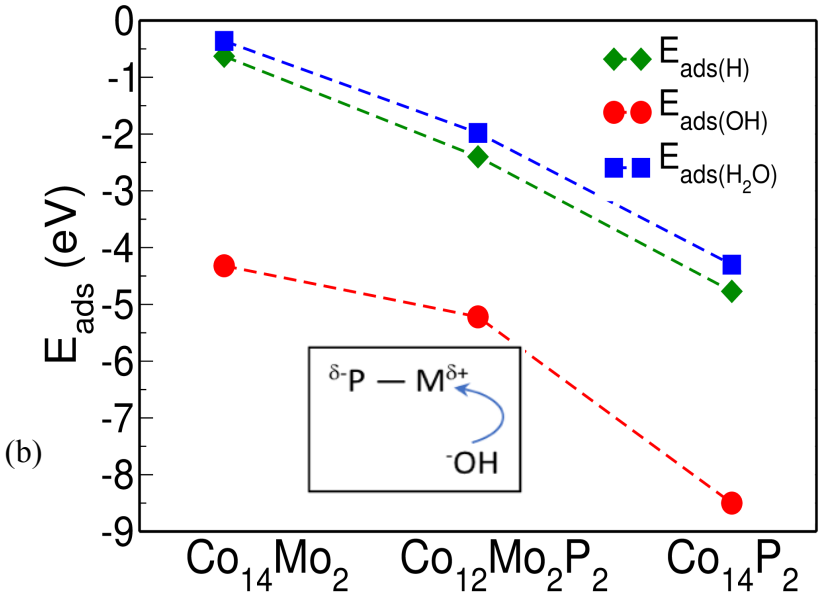
(b)
E_{ads} (eV)
$E_{ads(H)}$
$E_{ads(OH)}$
$E_{ads(H_2O)}$
$^{\delta-}$P — M$^{\delta+}$
$^{-}$OH
$Co_{14}Mo_2$
$Co_{12}Mo_2P_2$
$Co_{14}P_2$

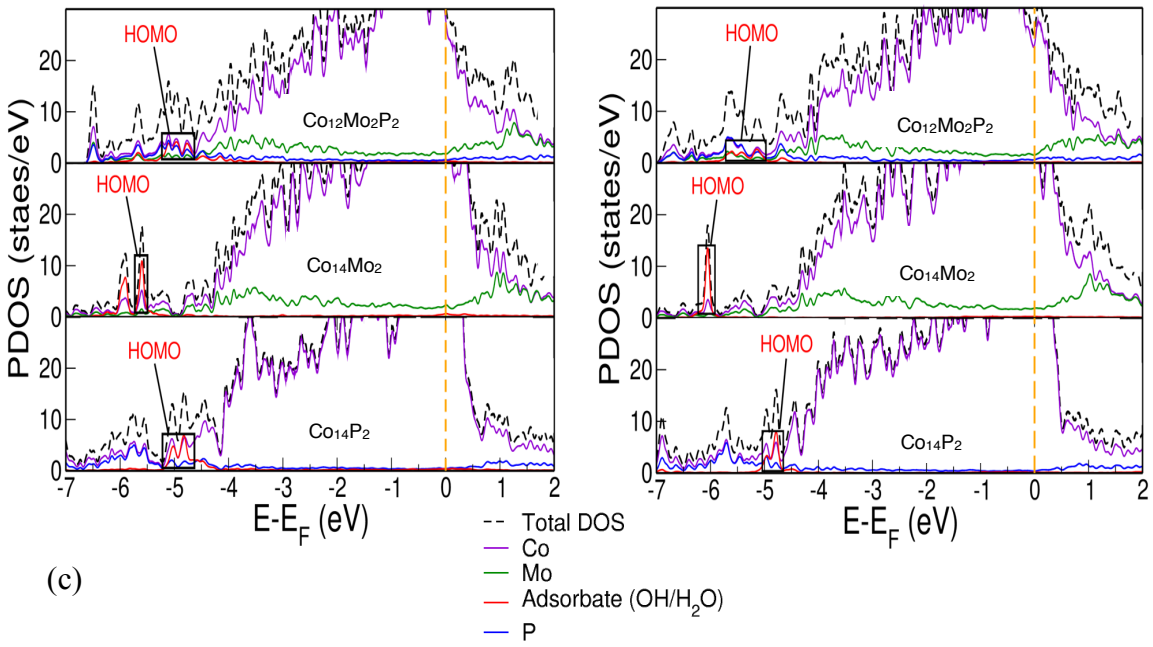
(c)
PDOS (staes/eV)
PDOS (states/eV)
HOMO
$Co_{12}Mo_2P_2$
$Co_{14}Mo_2$
$Co_{14}P_2$
E-E$_F$ (eV)
Total DOS
Co
Mo
Adsorbate (OH/H$_2$O)
P

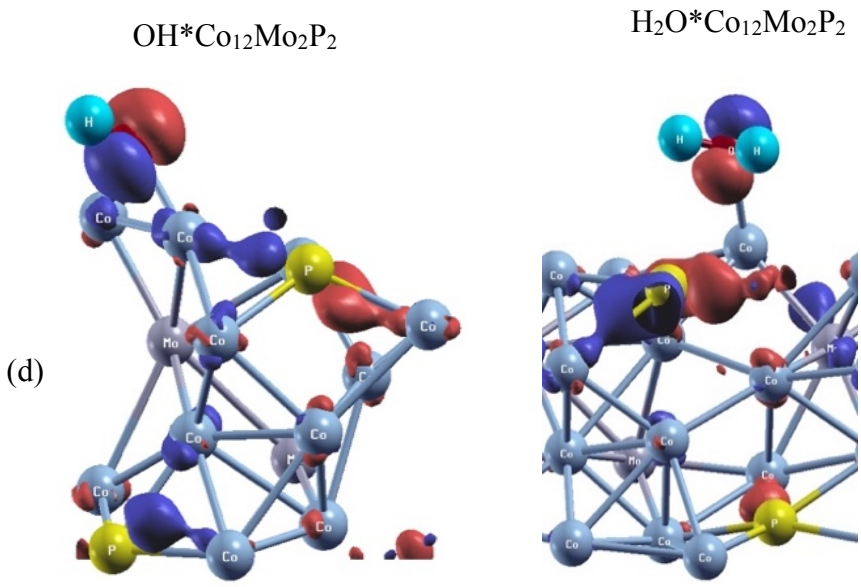

Fig. 4.5 (a) Splitting of H_2O molecules upon adsorption at the Mo-Co bridging site of (2x1x2) $Co_{28}Mo_4P_4$; **(b)** Energies of adsorption (E_{ads}) of H, OH and H_2O. Inset: A schematic showing the mechanism of how electronegative P-atom ionizes metal (M) and enhances -OH-binding; **(c)** PDoS of OH (top) and H_2O (bottom) adsorbed on $Co_{12}Mo_2P_2$, $Co_{14}Mo_2$, $Co_{14}P_2$; **(d)** Iso-surfaces of wave functions depicting the interacting orbitals (HOMO) for $OH^*Co_{12}Mo_2P_2$ and $H_2O^*Co_{12}Mo_2P_2$. Red and blue colors represent positive and negative iso-surfaces respectively. Co, Mo, P, O and H atoms are represented with blue, purple, yellow, red and cyan spheres respectively.

4.7 Conclusions

We simulate two model amorphous structures of Co-Mo-P alloy and examine their catalytic activity towards alkaline HER within the framework of density functional theory (DFT). To generate these structures, we employ expanding lattice method in which we construct a crystalline supercell expanded by 50%, relax it, leading to a nanoporous ($Co_{28}Mo_4P_4$) or disordered ($Co_{12}Mo_2P_2$) system. To quantify the catalytic performance of Co-Mo-P alloy, we determine the strength of adsorption of H-atom, H_2O molecule and OH at various surface sites. Our simulations of adsorption at various sites suggest that Co is the preferred site of adsorption of H. Upon adsorption of an H_2O molecule at Mo-Co bridging site, we find that the water molecule splits into H* and OH*. The H* and OH bind to Co and neighbouring Mo-Co bridging site respectively. Hence, we propose bridging Mo-Co as the active site for executing the *Volmer* step. On

comparing the OH adsorption on $Co_{12}Mo_2P_2$ to $Co_{14}Mo_2$ and $Co_{14}P_2$ we observe that the energies of adsorption of OH ($\Delta E_{ads(OH)}$) and H_2O ($\Delta E_{ads(H_2O)}$) on $Co_{14}P_2$ are higher than those on $Co_{14}Mo_2$. This effect is attributed to P being an electronegative element which ionizes a nearby metal atom, making it an attractive site for adsorption of an electron-rich species (like OH and H_2O). Mo in the Co-Mo-P alloy is responsible to weaken the H-binding which is shown by the decrease in $\Delta E_{ads(H)}$ in the case of $Co_{14}Mo_2$ as compared to both $Co_{14}P_2$ and $Co_{12}Mo_2P_2$. Thus, phosphorus site is key to facilitating the *Heyrovsky* step while molybdenum is responsible for the *Tafel* step. The synergy between Mo and P gives rise to the excellent catalytic activity of Co-Mo-P alloy in alkaline HER which is observed experimentally as well.

Bibliography

[1] Min Zeng and Yanguang Li, *J. Mater. Chem. A* **3**, 14942 (2015).

[2] P. Giannozzi *et al.*, *J. Phys. Condens. Matter* **21**, 395502 (2009); www.quantum-espresso.org.

[3] D. Vanderbilt, *Phys. Rev. B* **41**, 7892 (1990).

[4] J. P. Perdew, K. Burke, and M. Ernzerhof, *Phys. Rev. Lett.* **77**, 3865 (1996).

[5] H. W. King, CRC Handbook of Chemistry and Physics **83**, 19 (2002).

[6] Cristina Romero, Juan C. Noyola, Ulises Santiago, Renela M. Valladares, Alexander Valladares and Ariel A. Valladares, *Materials* **3**, 467-502 (2010).

[7] Ram Subbaraman, Dusan Tripovic, Dusan Strmcnik, Kee-Chul Chang, Masanobu Uchimura, Aryydas P. Paulikas, Vojislav Stamenkovic, Nenad M. Markovic, *Science* **334**, pp. 1256-1260 (2011).